Journal of Turbulence
Vol. 00, No. 00, 200x, 1–32

This paper is pubished in Journal of turbulence, available at:
http://dx.doi.org/10.1080/14685248.2017.1317923

Reynolds stress models applied to canonical shock-turbulence interaction

V. Jagadish Babu[a] and Krishnendu Sinha[b*]

[ab]*Department of Aerospace Engineering, Indian Institute of Technology Bombay, Mumbai, India 400076*

(*Received 00 Month 200x; final version received 00 Month 200x*)

Shock waves in high-speed flows can drastically alter the nature of Reynolds stresses in a turbulent flow. We study the canonical interaction of homogeneous isotropic turbulence passing through a normal shock, where the shock wave generates significant anisotropy of Reynolds stresses. Existing Reynolds stress models are applied to this canonical problem to predict the amplification of the streamwise and transverse normal Reynolds stresses across the shock wave. In particular, the efficacy of the different models for the rapid pressure-strain correlation is evaluated by comparing the results with available DNS data. The model predictions are found to be grossly inaccurate, especially at high Mach numbers. We propose physics-based improvement to the Reynolds stress transport equation in the form of shock unsteadiness effect [Sinha et al., Physics of Fluids, 15, 2003] and enstrophy amplification for turbulent dissipation rate [Sinha. K, Journal of Fluid Mechanics, 707, 2012]. The resulting model is found to capture the essential physics of Reynolds stress amplification, and match DNS data for a range of Mach numbers. Numerical error encountered at shock waves are also analyzed and the model equations are cast in conservative form to obtain physically-consistent results with successive grid refinement. Finally, the proposed model for canonical shock-turbulence interaction is generalized to multi-dimensional flows with shock of arbitrary orientation.

Keywords: RANS, turbulence models, shock waves, Reynolds stress anisotropy, shock unsteadiness.

1. Introduction

Shock-wave/turbulent boundary-layer interactions (SBLIs) are typical in aircraft propulsion systems, such as, scramjet engines. Interaction of the shock wave with the boundary layer results in regions of high pressure and thermal loads. The flow structure is altered due to the adverse pressure gradient created by the shock, and the boundary layer separates in the presence of strong shock waves. Unstart and severe structural damage, along with a reduction in vehicle performance are some of the drastic effects of uncontrolled SBLI. Accurate prediction of such flows is a challenging task and significant amount of research exists in literature [1–3].

In engineering predictions of SBLI problems, Reynolds-averaged Navier-Stokes (RANS) approach is generally used. Zheltovodov *et al.* [1], Roy *et al.* [2], and Gaitonde [3] reviewed the benefits and drawbacks of the numerical simulations. Canonical configurations, such as, compression ramps, sharp fins and impinging shock interactions have been extensively studied and the numerical predictions have been compared with experimental data. Various turbulence models based on eddy viscosity models, like, Spalart-Allmaras model, $k-\epsilon$ and $k-\omega$ models, Reynolds stress models (RSM) and RANS/Large eddy simulation (LES) hybrid methods have been employed in the simulations with varying degree of success.

*Corresponding author. Email: krish@aero.iitb.ac.in

ISSN: 1468-5248 (online only)

DOI: 10.1080/14685240YYxxxxxxx
http://www.tandfonline.com

Morgan *et al.* [4] investigated the cause of modeling errors in two-equation turbulence models and Reynolds stress models in prediction of the size of separation bubble and turbulence quantities. Hamlington and Dahm [5] modified the standard two-equation formulation to account for the flow history of the Reynolds stress tensor. Some other improvements in modeling of the unclosed terms in RSM for SBLI are reported in Vieira *et al.* [6] and Liu *et al.* [7]. Sinha *et al.* [8] modified the turbulent kinetic energy equation with shock unsteadiness correction and showed improvement over standard one- and two-equation turbulence models.

The canonical interaction of homogeneous isotropic turbulence with a nominally normal shock wave has been widely studied for its simplicity and rich physics. Compared to SBLI, complexities such as flow separation, streamline curvature, and boundary-layer velocity gradients are not present in this model problem. Canonical shock-turbulence interaction (STI) has been investigated using Direct numerical simulation (DNS) [9–11] and theoretical analysis tools, such as linear interaction analysis (LIA) and rapid distortion theory [11–14]. Physical insights obtained from such studies have been used to develop advanced turbulence models [14–17] for STI cases. When extended to SBLI problems, the models give better predictions compared to conventional models [18, 19].

An essential feature of STI is the anisotropic nature of Reynolds stresses generated downstream of the shock wave. An initially homogeneous isotropic disturbance field is converted into an axi-symmetric turbulence field by the normal shock. DNS data of Larsson *et al.* [9, 10] show the anisotropy in Reynolds stresses for a range of shock strengths. The Reynolds stresses in streamwise and transverse directions are amplified differently across the shock wave. Two-equation turbulence models like $k-\epsilon$ and $k-\omega$ cannot reproduce this shock induced anisotropy in Reynolds stresses, as they model the total effect of the amplification in the form of turbulent kinetic energy. On the other hand, models based on transport equations of individual Reynolds stresses are ideally suited to capture the anisotropic turbulence generated by the shock.

Compared to the two-equation models, RSMs have an extra pressure-strain correlation term, which models the redistribution of turbulent fluctuations uniformly in all directions. Earlier studies in second-moment closure models provide various types of approximations for the pressure-strain correlation terms [20–23]. Rotta [20] modeled the pressure-strain closure for decaying homogeneous turbulence without any mean strain in the flow. Extending Rotta's concept, Launder, Reece, and Rodi [21] proposed a general closure for the pressure-strain correlation, which is linear in the Reynolds stresses, and the model was referred to as Quasi-Isotropic (LRR-QI) model. Later, they proposed a different model by retaining the dominant term in the pressure-strain correlation; the simplified version is known as isotropization of the production (LRR-IP) Reynolds stress model. The rapid pressure-strain term tends to isotropize the turbulence production in this model.

Lumley [22] developed a nonlinear model for the pressure-strain correlation, which reduces to the LRR-QI model when the nonlinear anisotropy tensor terms are neglected. Using a different approach, Speziale, Sarkar, and Gatski (SSG) [23] postulated a quadratically nonlinear anisotropy tensor model. Adopting the LRR-IP model, Gibson and Launder [24] modified the pressure containing correlations by adding wall correction for the fluctuating pressure field. Later, Launder and Shima [25] proposed a new model extending the Gibson and Launder model to incorporate near-wall viscous sublayer effects by optimizing the model coefficients.

The closure models discussed above are for incompressible flows. For compressible flows, incompressible models are directly extended by replacing the Reynolds-averaged Reynolds stresses with Favre-averaged Reynolds stresses. Gerolymos *et al.*

[26–29] followed this approach for the Launder and Shima RSM by using modified dissipation equation from Launder-Sharma [30]. They developed three different models which are independent of geometry/wall topology. In [26] the coefficient of the rapid pressure-strain correlation term is retained. In [27], the coefficient is modified to provide a numerically robust model. Further improvements are made in [27] and the model [28] includes specific modeling for pressure-diffusion, non-linear inhomogeneous terms in the slow pressure-strain term model and a separate model for the dissipation rate tensor anisotropy. The models are applied to various flows, some of which are separated flows on supersonic compression ramps and three-dimensional shock-wave/boundary layer interaction [26–29, 31–33].

Taking into account the compressibility effects, Lee *et al.* [34] modified the pressure-strain correlation of the LRR-QI model and additionally considered dissipation-dilatation and the mass-averaged fluctuations. They applied the model to zero-pressure gradient supersonic turbulent boundary layers and to curved compression surfaces. A good match is observed for measured quantities like skin friction, mean velocity, and turbulent energy profiles with experimental results. In a similar approach, Ladiende [35] used the LRR-IP model with pressure-dilatation and dissipation-dilatation correction. The model was applied to supersonic turbulent boundary layers with adverse pressure gradient and found to give a good match with experimental results.

Gnedin and Knight [36] developed a model by extending the Rotta's model, with an additional compressibility correction term in the dissipation rate, proposed by Pantano and Sarkar [37], and Zeman [38]. Zha and Knight [39] adopted the Gnedin and Knight model and simulated three-dimensional crossing shock-wave/turbulent boundary-layer interactions. Heat transfer and pressure profiles are found to be in better agreement than the two-equation model when compared to experimental results. Wilcox [40] proposed a stress-transport model based on the Launder, Reece and Rodi's pressure-strain closure and specific dissipation rate, ω. The model was applied to shock-wave/boundary-layer interaction in compression corner and reflecting shocks, and the predictions are found to be better than standard two-equation models.

The objective of the present work is to evaluate existing Reynolds stress models in the canonical interaction of homogeneous isotropic turbulence with a nominally normal shock wave. The model predictions of the normal Reynolds stresses is compared with existing data from DNS of Larsson *et al.* [9, 10]. We propose improvements to the model transport equations based on the physics of the unsteady shock oscillations induced by the incoming turbulence. Numerical error at the shock waves is analysed and a robust conservative formulation is proposed. The new Reynolds stress model is found to match the DNS data over a range of Mach numbers. The effect of grid refinement and different numerical schemes on the turbulence amplification is presented, and the model equations are generalized to multi-dimensional flows with oblique shocks.

2. Governing equations

In the present work, Reynolds-averaged Navier–Stokes approach is adopted for compressible flows, and Favre decomposition is used for all terms except density and pressure. The transport equation for the Favre-averaged Reynolds stress tensor is

$$\frac{\partial \overline{\rho} R_{ij}}{\partial t} + \frac{\partial \overline{\rho} \widetilde{u}_l R_{ij}}{\partial x_l} = P_{ij} + \phi_{ij} + d_{ij} - \overline{\rho}\epsilon_{ij} + K_{ij} + \frac{2}{3}\phi_p \delta_{ij}, \tag{1}$$

where ρ is the density, $R_{ij} = \widetilde{u_i''u_j''}$ is the Reynolds stress tensor, δ_{ij} is the Kronecker delta, and $\widetilde{u}_i$ is the mean velocity. Tilde and overbar indicate Favre and Reynolds averaging, respectively, whereas double prime represents Favre fluctuation. The term on the left-hand side of Equation (1) represents the convection term.

The terms on the right side of Equation (1) are in order, production, pressure-strain correlation, diffusion, dissipation, direct compressibility effect, and pressure dilatation terms. $P_{ij} = -\overline{\rho}R_{jl}\widetilde{u_{i,l}} - \overline{\rho}R_{il}\widetilde{u_{j,l}}$ is the production of Reynolds stress due to mean velocity gradients, where $\widetilde{u_{i,l}}$ represents $\partial\widetilde{u}_i/\partial x_l$ and x_l denotes Cartesian space coordinates with $l = 1,2,3$. Here, the production term is in terms of Reynolds stresses and does not require modeling. The deviatoric part of the pressure-strain correlation term is given by $\phi_{ij} = \overline{p'(u''_{i,j} + u''_{j,i} - 2/3u''_{l,l}\delta_{ij})}$, where p is pressure and single prime indicates Reynolds fluctuation. It is decomposed into two parts depending on the type of contribution, namely, the slow and rapid pressure-strain terms. The slow pressure-strain term is also referred to as the return-to-isotropy term and represents turbulence–turbulence interaction. It is modeled as $\phi^s_{ij} = C_1\epsilon a_{ij}$ [20], where C_1 is a model coefficient and $a_{ij} = R_{ij}/k - 2/3\delta_{ij}$ is the anisotropy in Reynolds stresses; k and ϵ are the turbulent kinetic energy and its dissipation rate, respectively. This model is motivated from the homogeneous anisotropic turbulence decaying without any mean velocity gradients in the flow. The rapid pressure-strain term (ϕ^r_{ij}) responds directly to the change in mean velocity gradients. The importance of rapid pressure-strain term and its modeling is discussed briefly in the subsequent section.

Diffusion term $d_{ij} = (-\overline{\rho}\widetilde{u_i''u_j''u_l''} - \overline{p'u_j''}\delta_{il} - \overline{p'u_i''}\delta_{jl} + \mu R_{ij,l})_{,l}$ includes turbulent diffusive flux, pressure diffusion, and viscous diffusion. The turbulent and pressure diffusion terms are modeled by Daly and Harlow [41] using the generalised gradient diffusion hypothesis. Launder *et al.* [21] proposed an improved model for the triple correlation tensor, which is given as $\widetilde{u_i''u_j''u_k''} = -C_s(k/\epsilon)(R_{il}R_{jk,l} + R_{jl}R_{ki,l} + R_{kl}R_{ij,l})$, where C_s is 0.11. The viscous diffusion term is in the form of Reynolds stresses and does not require modelling. Possible numerical problem at shock due to Daly and Harlow [41] diffusion model have been discussed by Souffland *et al.* [42], where they present methods to minimize the numerical error.

The dissipation of Reynolds stresses at the smallest scales of turbulence due to viscous effects is represented as $\overline{\rho}\epsilon_{ij} = \overline{\sigma_{jl}u''_{i,l}} + \overline{\sigma_{il}u''_{j,l}}$, where σ_{jl} is the viscous stress. According to Kolmogorov's hypothesis, the smallest scales of motion are assumed to be isotropic and the dissipation tensor is modeled as $\epsilon_{ij} = \frac{2}{3}\epsilon\delta_{ij}$.

Favre-averaging introduces new terms in the transport equation involving mass-averaged velocity fluctuations and pressure-dilatation due to the deviatoric part of pressure-strain correlation. These terms have no counterpart in incompressible transport equations. Direct compressibility effects through variation in the density are represented by $K_{ij} = -\overline{u_i''}\,\overline{p_{,j}} - \overline{u_j''}\,\overline{p_{,i}} + \overline{u_i''}\,\overline{\sigma_{jl,l}} + \overline{u_j''}\,\overline{\sigma_{il,l}}$. Here, $\overline{u_i''}$ is related to the turbulent mass flux as $-\overline{\rho'u_i'}/\overline{\rho}$. It plays an important role in problems involving turbulent mixing [43, 44] and high-Mach number flows with significant thermodynamic fluctuations upstream of the shock wave [17]. In cases, where the upstream flow is dominated by vortical disturbances, as considered in this work, we can assume $\overline{u_i''}$ to be negligible. The last term, $\phi_p = \overline{p'u''_{l,l}}$ is the pressure dilatation term, and is modeled in terms of turbulent Mach number (M_t) by Pantano and Sarkar [37]. The contribution of the pressure dilatation is small compared to the production term for $M_t^2 \ll 1$, and can be neglected [14].

The transport equation for the turbulence dissipation rate is modeled as

$$\frac{\partial \overline{\rho}\epsilon}{\partial t} + \frac{\partial \overline{\rho}\widetilde{u_l}\epsilon}{\partial x_l} = -C_{\epsilon 1}\overline{\rho}R_{il}\frac{\epsilon}{k}\widetilde{u_{i,l}} - C_{\epsilon 2}\overline{\rho}\frac{\epsilon^2}{k} + C_{\epsilon}\overline{\rho}\frac{\partial}{\partial x_l}\left(\frac{k}{\epsilon}R_{il}\epsilon_{,l}\right), \tag{2}$$

and this form is used by all the Reynolds stress models discussed below. The terms on the right-hand side of this equation are, in order, production, dissipation, and diffusion terms. Here, $C_{\epsilon 1} = 1.44$, $C_{\epsilon 2} = 1.92$, and $C_{\epsilon} = 0.15$ are the empirical constants taken from Launder *et al.* [21]. The equation is analogous to Equation (1) except for the pressure-strain, mass averaged velocity fluctuation and pressure dilatation terms. Also, the diffusion term does not include the viscous and pressure diffusion effects. According to [45], the turbulent diffusion has a negligible effect across the shock, and it is neglected.

2.1. *Models for rapid pressure-strain correlation term*

The rapid pressure-strain term is directly proportional to the mean velocity gradient and is of the same form as the production term in Equation (1). It tends to redistribute the energy from the Reynolds stress component, where the production is significantly large compared to other components, consequently reducing the anisotropy in Reynolds stresses. The following are three turbulent closures for the rapid part of the pressure-strain correlation, which have been applied to compressible flows with shock waves.

The model proposed in Gerolymos *et al.* [26–28] is based on the isotropization of production in turbulence [21], and is given as

$$\phi^r_{ij} = -C_2(P_{ij} - \frac{2}{3}\delta_{ij}P). \tag{3}$$

Here $P = P_{kk}/2$, and the model coefficient C_2 is $0.75\sqrt{A}$ as per Gerolymos *et al.* [26] model, where the flatness parameter, $A = 1 - \frac{9}{8}(A_2 - A_3)$, with the anisotropy tensor invariants $A_2 = a_{ik}a_{ki}$ and $A_3 = a_{ik}a_{kj}a_{ji}$. For isotropic turbulence, the value of A is one as A_2 and A_3 tend to zero.

The rapid part of the pressure-strain term in the Zha and Knight [39] model is developed for isotropic turbulent flows subjected to sudden distortion (high mean strain). As per the model,

$$\phi^r_{ij} = C_{c2}\overline{\rho}kS_{ij}, \tag{4}$$

with C_{c2}=0.17, and $S_{ij} = \widetilde{u_{i,j}} + \widetilde{u_{j,i}}$. The model closure is a direct extension of the incompressible form, so the trace of ϕ^r_{ij} does not vanish for compressible flows.

Lee *et al.* [34] proposed a new formulation of the pressure-strain term, using the Poisson equation for pressure fluctuations in varying density flows. As per the model,

$$\begin{aligned}\phi^r_{ij} = &- C_{p2}(P_{ij} - \frac{2}{3}\delta_{ij}P) - C_3(D_{ij} - \frac{2}{3}\delta_{ij}P) \\ &- C_4k\overline{\rho}\left(S_{ij} - \frac{2}{3}S_{kk}\delta_{ij}\right) - C_5\overline{\rho}ka_{ij}\frac{\partial \widetilde{u}_l}{\partial x_l} + C_6\overline{\rho}R_{mm}\frac{\partial \widetilde{u}_l}{\partial x_l}\delta_{ij} \\ &+ \frac{1}{3}C_7P_k\delta_{ij},\end{aligned} \tag{5}$$

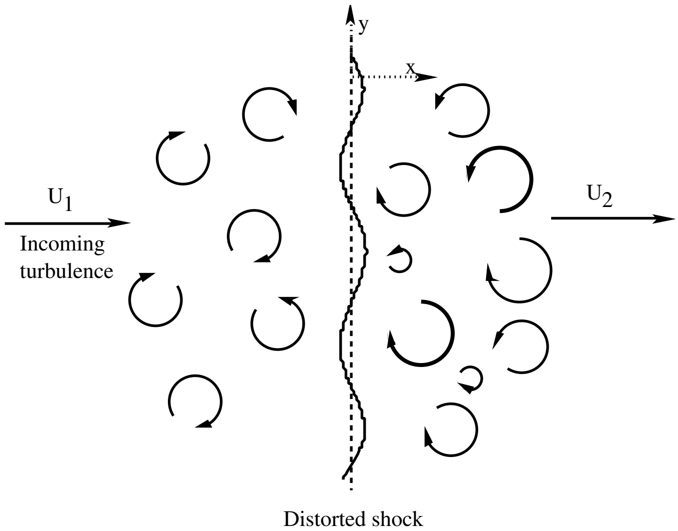

Figure 1. Schematic of homogeneous isotropic turbulence interacting with a normal shock wave distorted by the turbulent fluctuations passing through it.

where $D_{ij} = -\overline{\rho}R_{ik}\widetilde{u}_{k,j} - \overline{\rho}R_{jk}\widetilde{u}_{k,i}$, $C_{p2} = 0.76$, $C_3 = 0.10$, $C_4 = 0.18$, $C_5 = 0.14$, and $C_6 = 0.35$. The first three terms are identical to the LRR-QI model, and the following two terms are additional terms that arise due to mean dilatation. The last term is the production term generated by compressibility effect and is neglected [34].

All the above Reynolds stress closures use Rotta's [20] model for the slow pressure-strain term, where the model coefficient varies between different models. For Gerolymos *et al.* [26] model, the coefficient C_1 is given as $1 + 2.58AA_2{}^{\frac{1}{4}}\left[1 - exp\left[-\left(\frac{Re_T}{150}{}^2\right)\right]\right]$ and the value is 1 for isotropic turbulence. The coefficient of the slow pressure strain term for Zha and Knight [39] model is given as $C_{c1} = 4.325$ and the Lee *et al.* [34] model uses $C_{p1} = 1.5$. Here, Re_T is the turbulent Reynolds number.

2.2. *Canonical shock–turbulence interaction*

Canonical STI is the most fundamental problem where a one-dimensional mean flow carrying three-dimensional homogeneous isotropic turbulence interacts with a nominally normal shock (see figure 1). The shock wave amplifies the turbulence and makes it anisotropic. It also generates acoustic energy and causes a sudden change in the length scales of turbulence. The turbulent fluctuations passing through the shock make it unsteady, about its mean position, as shown in the figure. Thus, canonical shock turbulence interaction exhibits many of the important features of high-speed flows with shock waves. In this work, the upstream disturbance field is assumed to be purely vortical in nature, such that there are no pressure, density and temperature fluctuations in the incoming flow. This is the simplest model problem to isolate the shock physics on the turbulence field. High-speed flows can have non-negligible thermodynamic fluctuations, and their effect on the shock-turbulence interaction has been studied earlier [11, 17]. Other works related to shock-induced mixing can be found in [43, 44], where more general turbulence field is considered upstream of the shock wave. Figure 2(a) reproduced from Sinha [15] with permission shows the comparison of streamwise evolution of the turbulent kinetic energy computed by different turbulence models with DNS data. A normal shock wave with Mach number of 1.5 is located at $x = 3$. At the inlet station,

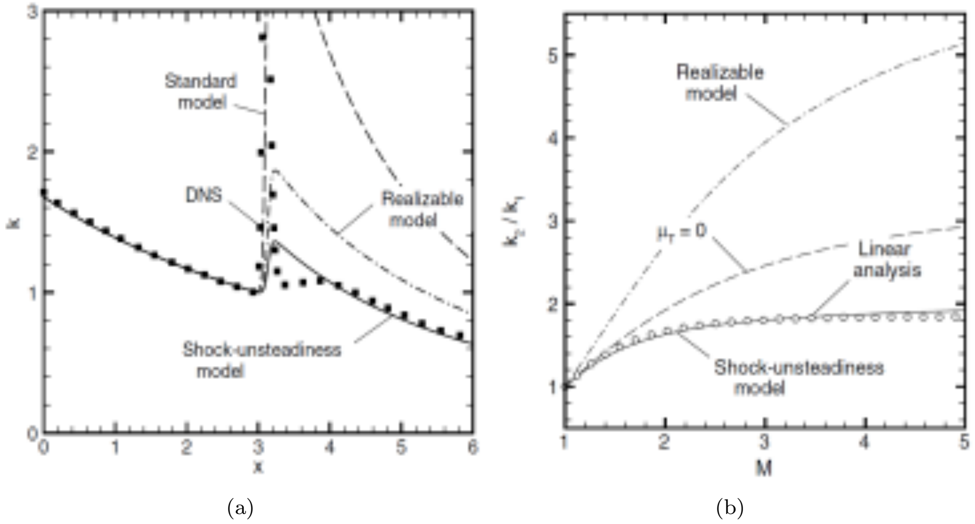

Figure 2. Amplification of turbulent kinetic energy in canonical shock turbulence interaction: (a) streamwise evolution in a Mach 1.5 interaction and (b) jump across shock waves for varying Mach numbers (reproduced from Sinha [15] with permission).

the values of Taylor microscale based Reynolds number and the turbulent Mach number are 6.7 and 0.17. The turbulent kinetic energy is normalized by its values immediately upstream of the shock wave. Upstream of the shock, turbulence dissipates from its inlet value due to zero mean velocity gradient and gets amplified across the shock. As a result of an increase in the dissipation rate of turbulence, the turbulent kinetic energy decays faster in downstream compared to upstream of the shock wave. At the shock, the DNS data shows very high value of the turbulent kinetic energy, which is due to unsteady motion of the shock and does not represent turbulence fluctuations. There is a non-monotonic variation in the turbulent kinetic energy immediately after the shock and the behaviour is due to the acoustic decay described by Mahesh *et al.* [11]. The standard $k-\epsilon$ model and realizable $k-\epsilon$ model overpredicts the DNS data, whereas the turbulent kinetic energy predicted by the shock-unsteadiness model shows good match with the DNS. The amplification of turbulent kinetic energy also matches well with linear theory for a range of Mach numbers shown in figure 2(b). The shock-unsteadiness modification has been incorporated into the $k-\omega$ model of Wilcox [40] and in SA turbulence model, and extended to SBLI problems. Two-dimensional SBLI flows, such as, supersonic compression corner [8], oblique shock impingement on turbulent boundary layer, and axisymmetric cone-flare [18, 19] were studied. In comparison with conventional models, the shock-unsteadiness model shows a significant improvement in predicting surface pressure, separation bubble size, and shock structure [18, 19].

2.3. *Simplified RSM for canonical shock–turbulence interaction*

The transport equations for the Reynolds stresses are simplified to a steady one-dimensional form applicable to the canonical STI problem considered in this work. Note that the equation for R_{33} is identical to that of R_{22} for the current model problem. For the Gerolymos *et al.* [26] model, equations for the shock-normal component R_{11} and transverse component R_{22} are given by

$$\widetilde{u}\frac{\partial R_{11}}{\partial x} = -2R_{11}\frac{\partial \widetilde{u}}{\partial x} + \frac{4}{3}C_2 R_{11}\frac{\partial \widetilde{u}}{\partial x} - C_1\epsilon a_{11} - \frac{2}{3}\epsilon, \tag{6}$$

$$\widetilde{u}\frac{\partial R_{22}}{\partial x} = -\frac{2}{3}C_2 R_{11}\frac{\partial \widetilde{u}}{\partial x} - C_1\epsilon a_{22} - \frac{2}{3}\epsilon, \tag{7}$$

where $\widetilde{u}$ is the shock-normal mean velocity in the x-direction. For isotropic turbulence, the coefficients reduce to $C_1 = 1$ and $C_2 = 0.75$. The first term on the right-hand side of Equation (6) represents production, the second and the third term constitute rapid and slow parts of pressure-strain correlation, and the last term represents turbulent dissipation. For the transverse Reynolds stress given by Equation (7), there is no production mechanism, that is, $P_{22} = P_{33} = 0$ (mean flow velocity gradient energizes the turbulence only in the axial component). The first two terms on the right-hand side of Equation (7) therefore represent rapid and slow parts of pressure-strain, and the last term represents dissipation. The pressure-strain term redistributes energy from the stream-wise Reynolds stress to the transverse Reynolds stresses, without affecting the turbulence kinetic energy.

For Zha and Knight [39] model, equations for R_{11} and R_{22} simplify to

$$\widetilde{u}\frac{\partial R_{11}}{\partial x} = -2R_{11}\frac{\partial \widetilde{u}}{\partial x} + C_{c2}\left(R_{11} + 2R_{22}\right)\frac{\partial \widetilde{u}}{\partial x} - C_{c1}\epsilon a_{11} - \frac{2}{3}\epsilon, \tag{8}$$

$$\widetilde{u}\frac{\partial R_{22}}{\partial x} = -C_{c1}\epsilon a_{22} - \frac{2}{3}\epsilon. \tag{9}$$

The R_{11} equation has terms similar to those in Equation (6), except for the contribution of both R_{11} and R_{22} in the rapid pressure-strain term. Comparing with Equation (7), the R_{22} equation has no rapid pressure-strain term (since $S_{22} = 0$). Therefore, the transverse Reynolds stresses R_{22} and R_{33} are not directly affected by the mean compression at the shock.

For Lee *et al.* model [34], the transport equations are given by

$$\widetilde{u}\frac{\partial R_{11}}{\partial x} = -2R_{11}\frac{\partial \widetilde{u}}{\partial x} + \left[\widehat{A}R_{11} + \widehat{B}R_{22}\right]\frac{\partial \widetilde{u}}{\partial x} - C_{p1}\epsilon a_{11} - \frac{2}{3}\epsilon, \tag{10}$$

$$\widetilde{u}\frac{\partial R_{22}}{\partial x} = \left[\widehat{C}R_{11} + \widehat{D}R_{22}\right]\frac{\partial \widetilde{u}}{\partial x} - C_{p1}\epsilon a_{22} - \frac{2}{3}\epsilon. \tag{11}$$

The coefficients of the rapid pressure-strain terms are grouped as, $\widehat{A} = \frac{4}{3}C_{p2} + \frac{4}{3}C_3 - \frac{2}{3}C_4 - \frac{2}{3}C_5 + C_6$, $\widehat{B} = \frac{2}{3}C_5 - \frac{4}{3}C_4$, $\widehat{C} = -\frac{2}{3}C_{p2} - \frac{2}{3}C_3 + \frac{1}{3}C_4 + \frac{1}{3}C_5 + C_6$, and $\widehat{D} = \frac{2}{3}C_4 - \frac{1}{3}C_5$. Across a normal shock, the contribution of the production and pressure-strain terms has the same form as in Equations (6) and (7), except for the contribution of both the Reynolds stresses in the rapid pressure-strain terms.

In the following sections, we apply the simplified RSM equations to the one-dimensional mean flow passing through a normal shock. The production and rapid pressure strain terms are active in the region of the shock wave (nonzero velocity gradient), while the dissipation rate and the slow pressure strain term determine the evolution of the Reynolds stresses in the downstream flow. Canonical shock-turbulence interaction thus provides a unique platform to assess existing turbulence models, both in terms of the Reynolds stress amplification across the shock and its downstream development. It brings out several key physics of the interaction, as discussed in section 2.2, and it is important for the turbulence models to capture these phenomena. Also, shock waves are numerical discontinuities in a flow simulation and therefore can be source of large numerical error. The simplified one-dimensional equations for the canonical STI are very useful in analyzing numerical characteristics of the model equations and eliminate large error in shock-dominated flows [15].

The objective of the paper is to develop a physically consistent and numerically robust Reynolds stress model for the canonical shock-turbulence interaction. We first isolate the physical modeling error in existing models (section 3) and propose physics-based improvements (sections 4.1 and 4.2) at shock waves. The procedure applied is such that it eliminates the numerical error from this evaluation. Once we have a physics-based model, we tackle the numerical aspects (in section 4.3) and develop a method to minimize numerical error at shock discontinuities. Finally, the proposed model equations are incorporated in a CFD solver and both the physical and numerical aspects of the new Reynolds stress model are assessed by detailed comparison with DNS data. Extension of the model equations to a general three-dimensional flow are described subsequently.

3. Model evaluation

3.1. *DNS data*

Larsson *et al.* [9, 10] present DNS data of the canonical STI problem for Mach numbers from 1.27 to 6 for varying turbulent Mach number, M_t, and Reynolds number based on Taylor microscale, Re_λ. The case with M_t in the range of 0.15–0.22, and $Re_\lambda = 40$ are considered for the present study. The normalized inlet values of the Reynolds stresses, turbulent kinetic energy, and dissipation rate are calculated from the DNS data, by considering the values (k_1 and ϵ_1) immediately upstream of the shock. The non-dimensional values of k_1, and ϵ_1 are calculated from

$$k_1 = \frac{{M_t}^2}{2}, \qquad \epsilon_1 = \frac{5{M_t}^3}{\sqrt{3}\kappa_0\lambda^* Re_\lambda}, \tag{12}$$

with $\kappa_0\lambda^* = 0.84$. The Taylor micro-scale is given by $\lambda^* = \sqrt{10\nu^* k^*/\epsilon^*}$ and the Reynolds number based on λ^* is defined as $Re_\lambda = \lambda^* u^*_{rms}/\nu^*$. The turbulence kinetic energy and its dissipation rate are normalized as $k = k^*/a^{*2}_\infty$, and $\epsilon = \epsilon^*/a^{*3}_\infty \kappa_0$. Here, a^*_∞ is the freestream speed of sound.

The shock-upstream values k_1 and ϵ_1 are extrapolated to the inlet station using the relation of homogeneous isotropic turbulence decaying without any mean strain. The relations are derived in [46], and given as

$$k_0 = k_1 \left[1 + \frac{x_{shk}\epsilon_0}{\widetilde{u_1} n k_0}\right]^n, \quad \epsilon_0 = \epsilon_1 \left[1 + \frac{x_{shk}\epsilon_0}{\widetilde{u_1} n k_0}\right]^{n+1}, \tag{13}$$

where, $n = 1/(C_{\epsilon 2} - 1)$ is the decay exponent with $C_{\epsilon 2} = 1.2$, and $x_{shk} = 6.83$ is the distance of shock from the inlet station, normalised with characteristic wave number κ_0. Subscripts 0 and 1 represent the inlet location and the location just upstream of the shock in the computational domain, which spans from the inlet at $x = -7.6$ to the exit at $x = 29.6$. For isotropic turbulence the Reynolds stresses are given as,

$$R_{11} = R_{22} = \frac{2}{3}k, \tag{14}$$

M	M_t	k_0 x 10^2	$R_{11,0}$ x 10^2	$R_{22,0}$ x 10^2	ϵ_0 x 10^3
1.27	0.15	1.48	0.992	0.992	0.421
1.5	0.15	1.45	0.969	0.969	0.410
1.87	0.22	2.78	1.85	1.85	1.08
2.5	0.22	2.66	1.77	1.77	1.04
3.5	0.22	2.60	1.73	1.73	1.00
4.7	0.22	2.55	1.70	1.70	0.978
6.0	0.22	2.52	1.68	1.68	0.964

Table 1. Normalised values of the turbulent kinetic energy, streamwise and transverse Reynolds stresses and the turbulent dissipation rate at the inlet location for varying shock strengths in the canonical shock–turbulence interaction.

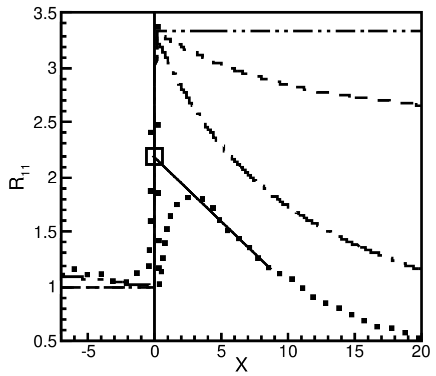

(a) R_{11}

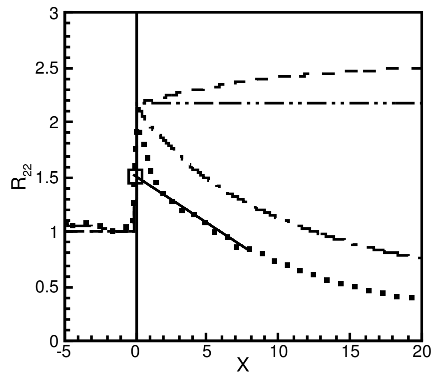

(b) R_{22}

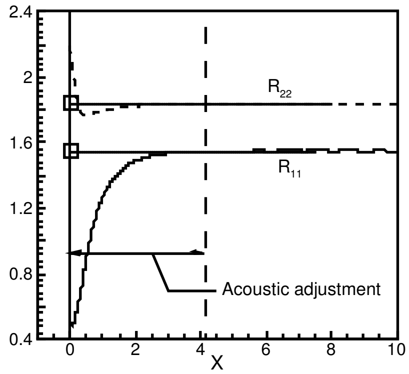

(c) R_{11} & R_{22} from LIA

Figure 3. Streamwise evolution of the turbulence quantities in a Mach 2.5 canonical STI. Numerical solution computed for the baseline (dash-dot), baseline model without dissipation term (dashed) and baseline model without the slow pressure strain and dissipation terms (dash-dot-dot) are compared with the DNS data (symbol). The post-shock Reynolds stresses predicted by the linear interaction analysis (LIA) are plotted in (c), where the LIA results are obtained using the procedure described in Quadros *et al.* [47].

and the Reynolds stresses are normalized in a way similar to the turbulent kinetic energy. The non-dimensional values of the Reynolds stresses and the dissipation rate are calculated from the baseline inlet conditions and are tabulated in table 1.

Figure 3 show streamwise evolution of R_{11} and R_{22} for the DNS data, where the Reynolds stresses are scaled by the respective shock-upstream values. In the unsteady shock region, the DNS data for R_{11} takes very high values and outside, it rapidly increases from a low post-shock value to reach a local maximum at $x = 4$. This corresponds to the acoustic adjustment region in LIA (see figure 3(c)), where R_{11} increases due to the post-shock redistribution between the vortical and acoustic fluctuations. In the absence of viscous and non-linear effects in LIA, the Reynolds stresses reach asymptotic far-field values, whereas the DNS data shows a monotonic decay far away from the shock ($x > 4$). The transverse Reynolds stress R_{22} has a peak at the shock, followed by a rapid decrease in the acoustic adjustment region to reach the far-field value.

The extent of the acoustic adjustment region in the shock-turbulence interaction is about one wavelength of the most-energetic upstream wave number. This is equivalent to the integral scale of turbulence upstream of the shock wave, approximately equal to one boundary layer thickness in a shock-boundary layer interaction. In a practical application, this region is expected to be small and the far-field values away from the shock are important. We extrapolate the monotonic decay in R_{11} and R_{22} (see figure 3) back to the shock center to obtain an equivalent far-field value from the DNS. This value is shown by an open square at $x = 0$ and it serves as a benchmark for model evaluation, as discussed in the subsequent section. The extrapolated value includes the jump in Reynolds stresses at the shock as well as the net effect of acoustic adjustment in the region immediately following the shock wave.

The Reynolds stress model Equations (6) and (7) applied to a Mach 2.5 shock-turbulence interaction, is shown in figures 3(a) and 3(b) for comparison with DNS data. The model transport equations include the production and rapid pressure strain terms that are active in the region of non-zero mean velocity gradient. They lead to a jump in R_{11} and R_{22} across the shock wave, as shown by the dashed-dot-dot line in the plots obtained by neglecting the dissipation and slow pressure strain terms in the model equations. The viscous dissipation results in a monotonic decay both upstream and downstream of the shock. On the other hand, the slow pressure strain term is responsible to make the post-shock field isotropic. It leads to a decrease in R_{11} and an increase in R_{22} behind the shock; compare the dashed lines in figures 3(a) and 3(b) with those obtained by neglecting the slow pressure strain term. The effect is qualitatively different from the acoustic adjustment of the Reynolds stresses observed in the DNS and LIA, where R_{11} increases and R_{22} decreases with distance from the shock wave. In addition, the slow pressure strain term acts over a much larger length scale than the acoustic adjustment region in the STI and can be effectively represented as a modification of the viscous decay rates of R_{11} and R_{22} in the post-shock flow. The effect of the viscous dissipation and the slow pressure strain terms is therefore neglected in evaluating the model capability in predicting the rapid changes in R_{11} and R_{22} in the vicinity of the shock wave.

3.2. *Reynolds stress amplification*

Figure 4 compares the amplification of R_{11} and R_{22} obtained from the DNS and the RSM equations for a range of shock strengths. The DNS data corresponds to the extrapolated shock values, and include the jump as well as the net effect of the rapid acoustic adjustment immediately downstream of the shock wave. The model predictions are obtained by considering only the production and rapid pressure strain terms in the transport equations for R_{11} and R_{22}. Neglecting the dissipation and slow pressure-strain terms do not affect the R_{11} and R_{22} amplifications predicted in 3(a) and 3(b). For the Gerolymos *et al.* [26] model, the equations can thus be integrated to get a closed form solution for the Reynolds stress amplifications across the shock wave.

$$\frac{R_{11d}}{R_{11u}} = \left[\frac{\widetilde{u}_u}{\widetilde{u}_d}\right]^{2-\frac{4}{3}C_2}, \tag{15}$$

$$\frac{R_{22d}}{R_{22u}} = 1 + \frac{C_2}{3-2C_2}\left[\frac{R_{11d}}{R_{11u}} - 1\right], \tag{16}$$

with subscripts u and d denoting the locations upstream and downstream of the shock respectively.

Neglecting the dissipation and slow pressure-strain terms, the R_{11} equation of the Zha and Knight [39] model reduces to,

$$\widetilde{u}\frac{\partial R_{11}}{\partial x} = \left[(-2 + C_{c2})R_{11} + 2C_{c2}R_{22u}\right]\frac{\partial \widetilde{u}}{\partial x}, \tag{17}$$

where the upstream value of the transverse Reynolds stress R_{22u} is used in the above equation, as it remains constant across the shock as per Equation (9) without the dissipation and slow pressure strain terms. In the Lee *et al.* [34] model, the Reynolds stress transport equations retaining the production and rapid pressure-strain terms, are given as,

$$\widetilde{u}\frac{\partial R_{11}}{\partial x} = \widehat{A}R_{11}\frac{\partial \widetilde{u}}{\partial x} + \widehat{B}R_{22}\frac{\partial \widetilde{u}}{\partial x}, \tag{18}$$

$$\widetilde{u}\frac{\partial R_{22}}{\partial x} = \widehat{C}R_{11}\frac{\partial \widetilde{u}}{\partial x} + \widehat{D}R_{22}\frac{\partial \widetilde{u}}{\partial x}, \tag{19}$$

with the constants $\widehat{A} = -0.70$, $\widehat{B} = 0.14$, $\widehat{C} = -0.12$, and $\widehat{D} = 0.07$. Across the shock, Equations (17), (18), and (19) do not give closed-form solutions for the amplification of turbulence quantities. We numerically integrate these equations using 4^{th} order accurate Runge–Kutta method for a specified mean flow profile across the shock wave. It can be shown that the results of the integration does not depend on the specified mean profile. The proof relies on switching from the physical space to local compression space and is used in [44]. Figure 4 plots the amplification of Reynolds stresses, dissipation rate, and the anisotropy in Reynolds stresses obtained using different models. The DNS data shows that R_{11} amplifies across the shock upto Mach 2.5 and attains a peak amplification value of 2.15. For Mach numbers greater than 2.5, the amplification reduces from the peak value and saturates at a value of 2.0 across the shock. The amplification of the streamwise Reynolds stress, R_{11}, from the Zha and Knight [39] RSM predicts very high values for all Mach numbers. The R_{11} amplifications in the Gerolymos *et al.* [26] and Lee *et al.* [34] models, show increasing values before asymptotically reaching a constant value at high Mach numbers. Both the models have a good match with the DNS data at lower Mach numbers up to 1.87, beyond which they overpredict by upto a factor of 2.5. We note that the Gerolymos *et al.* [26] model results correspond to $C_2 = 0.75$, and the alternate forms of the model with $C_2 = 1$ proposed by [27], [28], would further overpredict the R_{11} amplification.

Similar to R_{11}, the DNS data shows amplification in R_{22}, which gradually increases upto Mach 2.5 and saturates at a value of 1.7 for high Mach numbers. The amplification in R_{22} is monotonic across the shock for varying shock strengths, unlike R_{11}, which decreases slightly at high Mach numbers. Unlike the DNS data, the Zha and Knight [39] RSM predicts a constant value for all Mach numbers. The Gerolymos *et al.* [26] model overpredicts the DNS data by upto a factor of 2,

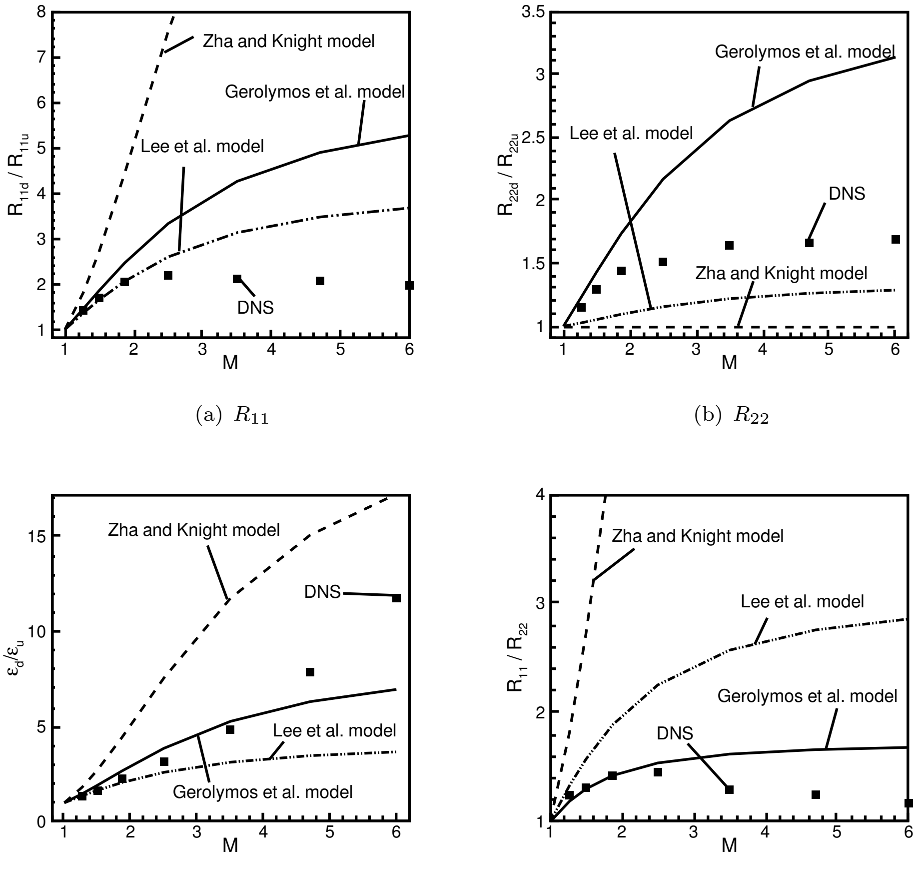

(a) R_{11} (b) R_{22}

(c) ϵ (d) R_{11}/R_{22}

Figure 4. The amplification of R_{11}, R_{22}, ϵ and anisotropy(R_{11}/R_{22}) across the normal shock for varying Mach number, as obtained from DNS data [9, 10] and different Reynolds stress models.

whereas the Lee *et al.* [34] model underpredicts the R_{22} amplification; these two models indicate a gain in R_{22} from R_{11}, due to redistribution of energy. The Zha and Knight [39] model, on the other hand, yields no R_{22} amplification because of the reason mentioned earlier.

In figure 4(c), the amplification of the dissipation rate from the DNS data is shown; it increases steadily with increasing Mach number. In contrast, for all of the RSMs considered, the dissipation rate increases monotonically and saturates at high Mach numbers. The Gerolymos *et al.* [26] model predictions are comparable to the DNS amplification of ϵ up to Mach 3.5. On the other hand, the Lee *et al.* and Zha and Knight models underpredict and overpredict the ϵ jump by large factors for almost all the Mach numbers.

In the DNS data, the anisotropy of Reynolds stresses across the shock is seen to increase upto Mach number 1.87 and then decrease significantly at higher Mach numbers. For all RSMs, the anisotropy across the shock behaves similar to R_{11} amplification and does not reproduce the non-monotonic variation observed in the DNS data. The Zha and Knight [39] RSM and Lee *et al.* [34] RSM overpredict the anisotropy for all Mach numbers by factors larger than 2. The Gerolymos *et al.* [26] model shows a good match with the DNS data upto Mach number 2, but overpredicts for higher Mach numbers. Gerolymos *et al.* [26] model is considered for further development and it will be referred to as the baseline model in the subsequent sections.

4. Physics based model improvement

Sinha *et al.* [14] studied the amplification of turbulence in a canonical shock-turbulence interaction using linear interaction analysis (LIA). In this approach, the inviscid shock wave is treated as a discontinuity and the upstream turbulence field is decomposed into Fourier modes. The elementary interaction of a two-dimensional plane wave with the deformed and unsteady normal shock wave forms the heart of this theory. For a given upstream Mach number and plane wave incidence angle, the theory predicts the disturbance waves generated downstream of the shock. Superposition of the single wave results for a specified upstream energy spectrum yields the downstream statistics for three-dimensional turbulence [11].

The fluctuating velocity field in a turbulent flow interacts with the normal shock, making the shock oscillatory and unsteady in nature. Conventional RANS models do not consider the shock oscillations, and give a very high amplification of turbulent kinetic energy at the shock wave. To incorporate the effect of shock-unsteadiness, Sinha *et al.* [14] derived the transport equation for the turbulent kinetic energy by linearising the governing equations about the unsteady distorted shock wave. Here, the reference coordinate frame is attached to the instantaneous shock, and the turbulent fluctuations are assumed to be small compared to the changes in the mean flow quantities. The deviation of the shock wave from its mean location is represented by $x = \xi(y, z, t)$, and the temporal derivative, ξ_t, represents the instantaneous speed of the shock wave.

4.1. *Streamwise and transverse Reynolds stress*

In the inviscid framework, the transport equation of $\widetilde{u''^2}$ for homogeneous isotropic turbulence interacting with a normal shock is given by [14],

$$\overline{\rho}\widetilde{u}\frac{\partial \widetilde{u''^2}}{\partial x} = -2\overline{\rho}\widetilde{u''^2}\frac{\partial \widetilde{u}}{\partial x} + 2\overline{\rho}\widetilde{u''\xi_t}\frac{\partial \widetilde{u}}{\partial x} - 2\overline{u''}\frac{\partial \overline{p}}{\partial x} - 2\overline{u''\frac{\partial p'}{\partial x}}.$$

This is an exact transport equation for R_{11} and it is derived for one-dimensional flow through a oscillating normal shock. It is written in a frame of reference attached to the unsteady shock wave. Additionally, non-linear and higher order terms are neglected by assuming that the fluctuations are small in magnitude compared to the jump in the mean flow quantities across the shock. The terms on the right hand side of the equation are in order, the production due to mean compression, the shock-unsteadiness effect, the production due to mean pressure gradient, and the velocity-pressure correlation. The shock-unsteadiness term is found to be responsible for reduction in the amplification of the turbulent kinetic energy across the shock [14].

The correlation $\widetilde{u''\xi_t}$ represents the coupling between the unsteady shock motion and the turbulent velocity fluctuations in the streamwise direction. The closure model for the unclosed term $\widetilde{u''\xi_t}$ was proposed to be of the form $b_1\widetilde{u''^2}$ based on the assumption that shock-unsteadiness is caused by turbulent fluctuations. Using linear analysis, the model coefficient, b_1, is obtained as a function of the upstream mean flow Mach number (M_{1n}) with respect to the normal shock. The model parameter b_1 is further modified to b_1' such that the turbulent kinetic energy amplification across the shock matches the limiting behaviour as $M_{1n} \to 1$ and $M_{1n} \to \infty$.

$$b_1' = b_{1\infty}\left(1 - e^{1-M_{1n}}\right), \tag{20}$$

where $b_{1\infty} = 0.4$ is the high Mach number limiting value of b_1 as obtained from LIA. Comparison of the shock unsteadiness model with the available DNS data yields a good match for the amplification of turbulent kinetic energy across the shock wave [14, 16].

In the present study, the shock-unsteadiness correction term is incorporated into the streamwise Reynolds stress equation of the baseline model [26]. The modified equation in written as,

$$\widetilde{u}\frac{\partial R_{11}}{\partial x} = (-2 + 2b_1' + \frac{4}{3}C_2)R_{11}\frac{\partial \widetilde{u}}{\partial x} - C_1\epsilon a_{11} - \frac{2}{3}\epsilon, \tag{21}$$

which is identical to Equation (6), except for the shock-unsteadiness damping term with model coefficient b_1' given above.

We evaluate the model in two steps. First, we compare the model predictions across the shock with the post-shock values of the DNS data extrapolated back to the shock wave. For this, we consider the production and rapid pressure strain terms that are effective in the shock region and obtain a closed-form solution for the shock-jump in R_{11} and R_{22}. Comparison with the extrapolated DNS values assesses the efficacy of the model in capturing the jump across the shock and the net change in R_{11} and R_{22} due to the rapid post-shock acoustic adjustment. As noted earlier, the acoustic adjustment region is relatively small in size (for a realistic application) and its effect can be combined with the shock jump in Reynolds stresses. Also, the slow pressure strain term is neglected in this comparison, as it does not reproduce the physical effects observed in the acoustic adjustment region.

As a second step, we solve the entire transport equations and compare the streamwise evolution of the Reynolds stresses with the DNS data (section 5.3). We also assess the effect of numerical error at the shock (in section 4.3) and device ways to eliminate them. We note that the shock-jump predicted by the complete model equation (in section 5.3) matches the analytical results obtained by considering only the production and rapid pressure strain terms. By comparison, the decay of Reynolds stresses away from the shock (outside the acoustic adjustment region) is governed by the dissipation rate and the slow pressure strain terms, which is modeled in terms of ϵ. The two stage evaluation of the Reynolds stress models, along with the extrapolation of the DNS data to the shock-center location, thus isolates the rapid effects at the shock wave from the slow decay and return to isotropy farther away from the shock. A similar procedure is adopted for the dissipation rate equation as well. Neglecting the slow pressure-strain and dissipation rate terms in the R_{11} equation (cf. Equation 21), a closed-form solution for the amplification of R_{11} across the shock is obtained as

$$\frac{R_{11d}}{R_{11u}} = \left[\frac{\widetilde{u}_u}{\widetilde{u}_d}\right]^{2(1-b_1')-\frac{4}{3}C_2}. \tag{22}$$

It is plotted in figure 5(a) as a function of the upstream Mach number and compared with the DNS data and the baseline model [26]. The amplification of R_{11} obtained with the new model has a trend similar to the DNS data and saturates to the value of 2.1 at high Mach numbers. The new model matches the DNS data upto Mach number 2.5 and slightly overpredicts the post-shock R_{11} for higher Mach numbers. The shock-unsteadiness damping term thus shows a significant improvement, compared to the baseline model, in the prediction of post-shock streamwise Reynolds stress.

In the new model, the value of the model coefficient, C_2, is reduced to 0.55 from the baseline model coefficient of $0.75\sqrt{A}$. This value compares well with $C_2 =$

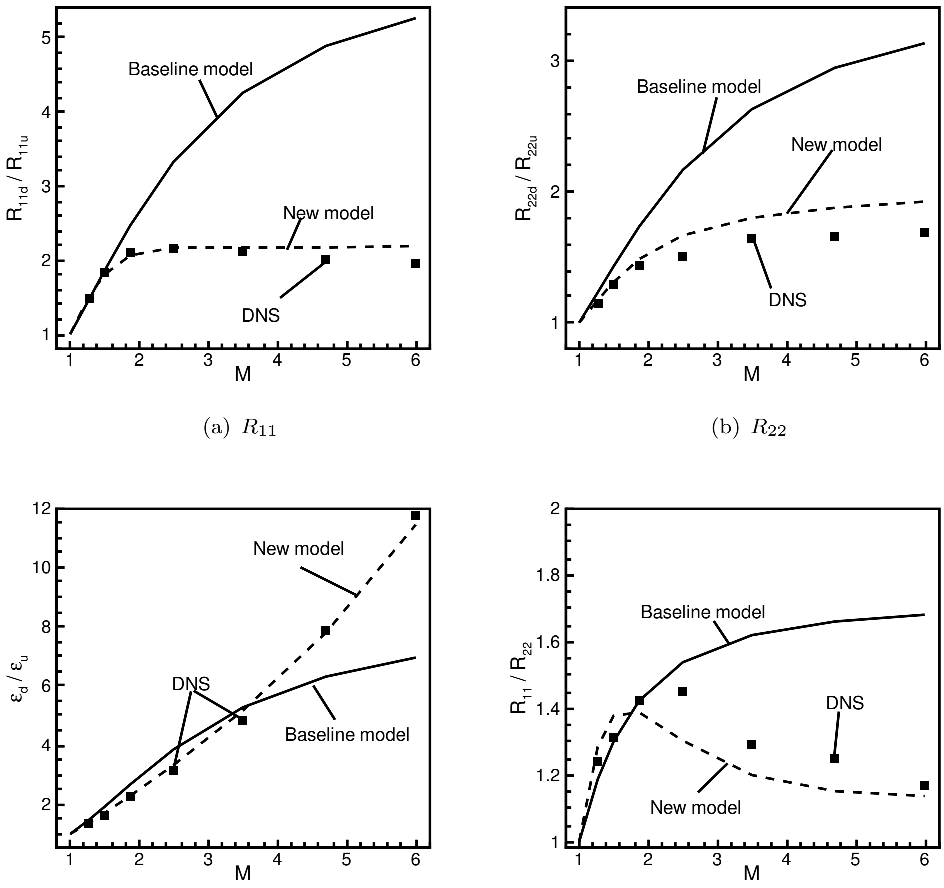

(a) R_{11} (b) R_{22}

(c) R_{11}/R_{22} (d) ϵ

Figure 5. Comparsion of the amplification in the R_{11}, R_{22}, ϵ, and anisotropy (R_{11}/R_{22}) of the baseline model (solid-line) and the present model (dash) with the DNS data (symbols) for varying shock strengths.

0.6 in the Launder *et al.* [21] model for isotropic turbulence subjected to rapid distortion. Limiting the value of C_2 improves the R_{11} predictions and leads to a close comparison with the DNS data for R_{22} amplification across the shock wave, as shown below.

The transverse Reynolds stress equation in the new model retains the same form as Equation (7). The closed-form solution for the amplification of R_{22} across the shock is thus given by

$$\frac{R_{22d}}{R_{22u}} = 1 + \frac{C_2}{3(1-b_1') - 2C_2}\left[\frac{R_{11d}}{R_{11u}} - 1\right]. \tag{23}$$

Compared to the closed-form solution in Equation (16), the R_{22} amplification obtained from the above equation includes the effect of shock-unsteadiness (through a model parameter b_1'). In comparison with the baseline model, the R_{22} amplification of the new model shows significant improvement, in figure 5(b). The effect of shock-unsteadiness damping factor in R_{11} is also observed in the R_{22} amplification. The transverse Reynolds stress has a good match with the DNS data upto Mach 1.87, beyond which it overpredicts the amplification across the shock by about 10%. In figure 5(c), the anisotropy of Reynolds stresses predicted by the new model shows the non-monotonic behaviour observed in the DNS data, and is a significant improvement from the baseline model. Comparison with the DNS data, shows that the new model overpredicts the anisotropy of Reynolds stresses for lower Mach numbers and underpredicts beyond Mach number 2.

4.2. *Turbulent dissipation rate*

The dissipation rate for any turbulent flow determines the rate of decay of the turbulent quantities. In compressible flows, the dissipation rate is divided into two parts, a solenoidal part, ϵ_s and a dilatational part, ϵ_d. For incompressible homogeneous turbulence, the solenoidal dissipation rate ϵ can be written in terms of enstrophy and is given by $\epsilon_s = \overline{\nu\omega_i''\omega_i''}$, where ν is the kinematic viscosity and ω_i is the vorticity component in the x_i direction. In the linear framework, the difference between the Reynolds averaging and Favre averaging is negligible. Here standard Reynolds averaging is used for compressible flows. Sinha *et al.* [16] derived the enstrophy equation from the linearised Navier–Stokes equations. The equations are written in a frame of reference attached to the unsteady shock wave, and are modeled as

$$\overline{u}\frac{\partial}{\partial x}(\overline{\omega_i''\omega_i''}) = -4\overline{\omega_z''^2}\frac{\partial\widetilde{u}}{\partial x} = -c_w\overline{\omega_i''\omega_i''}\frac{\partial\widetilde{u}}{\partial x}. \tag{24}$$

Here, the lower and upper limits of the model constant c_w is set by $\frac{\overline{\omega_i''\omega_i''}}{3} \leq \overline{\omega_z''^2} \leq \frac{\overline{\omega_i''\omega_i''}}{2}$, and a value of $c_w = 1.55$ shows a close match with linear analysis results [16].

The model equation for the solenoidal dissipation rate is thus written as,

$$\widetilde{u}\frac{\partial\epsilon_s}{\partial x} = \widetilde{u}\frac{\partial}{\partial x}(\overline{\omega_i''\omega_i''}\overline{\nu}) = \widetilde{u}\overline{\omega_i''\omega_i''}\frac{\partial\overline{\nu}}{\partial x} + \widetilde{u}\,\overline{\nu}\frac{\partial(\overline{\omega_i''\omega_i''})}{\partial x}, \tag{25}$$

where the dynamic viscosity, $\overline{\mu}$ is a function of mean temperature $\widetilde{T}$, and is given by $\overline{\mu} \propto \widetilde{T}^\alpha$ with α= 0.76. Across the shock, the change in kinematic viscosity is given as,

$$\frac{\partial\overline{\nu}}{\partial x} = -\frac{\overline{\mu}}{\overline{\rho}^2}\frac{\partial\overline{\rho}}{\partial x} + \frac{1}{\overline{\rho}}\frac{\partial\overline{\mu}}{\partial x} = \overline{\nu}\left[\frac{1}{\widetilde{u}}\frac{\partial\widetilde{u}}{\partial x} + \frac{\alpha}{\widetilde{T}}\frac{\partial\widetilde{T}}{\partial x}\right]. \tag{26}$$

Upon substitution of the change in kinematic viscosity in to the equation for solenoidal dissipation rate, we get

$$\widetilde{u}\frac{\partial\epsilon_s}{\partial x} = -c_w\epsilon_s\frac{\partial\widetilde{u}}{\partial x} + \epsilon_s\frac{\partial\widetilde{u}}{\partial x} + \alpha\epsilon_s\frac{\widetilde{u}}{\widetilde{T}}\frac{\partial\widetilde{T}}{\partial x}. \tag{27}$$

Using conservation of total enthalpy across the shock, the above equation is cast in a form similar to that in the conventional turbulence model as,

$$\overline{\rho}\,\widetilde{u}\frac{\partial\epsilon_s}{\partial x} = -\frac{2}{3}C_{\epsilon 1}\overline{\rho}\epsilon_s\frac{\partial\widetilde{u}}{\partial x} - C_{\epsilon 2}\overline{\rho}\frac{{\epsilon_s}^2}{k}, \tag{28}$$

where, $C_{\epsilon 1} = 1 + 0.21M_1$, and $C_{\epsilon 2} = 1.2$ taken from [16]. The closed-form solution for the amplification of ϵ across the shock is obtained by neglecting the last term.

$$\frac{\epsilon_d}{\epsilon_u} = \left[\frac{\widetilde{u_u}}{\widetilde{u_d}}\right]^{\frac{2}{3}C_{\epsilon 1}}. \tag{29}$$

The dissipation rate of the new model has excellent agreement with the DNS data (see figure 5(d)), both qualitatively and quantitatively, for all the Mach numbers.

4.3. *Numerical error at the shock*

The new model equations of the Reynolds stresses and the dissipation rate are not in conservative form. The non-conservative nature of the equations is due to the product of the mean flow variable and the derivatives in the source terms, as in Equation (21). The non-conservative source terms can lead to large numerical error at a shock wave. The amplification of turbulent quantities can thus show a non-physical trend.

Sinha and Balasridhar [15] studied the numerical issues in shock–turbulence interactions using the shock-unsteadiness $k - \epsilon$ turbulence model equations. The convective terms in the $k - \epsilon$ equations are written in a conservative form, such that the integrated error can be written in terms of the derivatives evaluated at the cell interfaces. By taking all the cells spanning the region of shock together, the error contribution gets cancelled at the common interface of adjacent cells. The net error across the shock wave is thus given by the higher-order derivatives calculated outside the shock wave, where the flow solution is smooth. With successive increment in grid points, the leading-error term vanishes, and the solution tends towards the exact solution.

The leading truncation error for the production term exhibit a different behaviour. Their contribution from adjacent cells adds up and lead to non-physical nature of the amplification of turbulent quantities. The leading error term for production due to mean compression scales as $1/\delta^3$. Here, δ is the shock thickness and it depends on the grid cell size, such that grid refinement increases the error further. A detailed analysis of numerical error at the shock wave is presented in the appendix of Sinha and Balasridhar [15].

To minimize the numerical truncation error at the shock wave, Sinha and Balasridhar [15] proposed an conservative form of the shock-unsteadiness $k - \epsilon$ model, obtained by transforming the turbulence variables to conserved quantities. New conserved variables involving k and ϵ are formulated, and the respective transport equations for the model problem are derived. The new equations represent identical physics as that of the original shock-unsteadiness model and are free from the numerical error due to the non-conservative source terms. The results of the conservative form of the shock-unsteadiness model, qualitatively and quantitatively match with the analytically integrated solution, and also show a good match with DNS data [15].

Similar to the $k - \epsilon$ model equations, Equations (21), (7), and (28), show non-conservative nature. Following an approach similar to that of Sinha and Balasridhar [15], the turbulent quantities are transformed to conserved quantities. Considering the exact solution in the inviscid limit given by Equations (22), (23), and (29), the new transformed turbulent variables are framed as,

$$\begin{aligned} f_1 &= R_{11}\rho^{2(b_1'-1)+4C_2/3}, \\ f_2 &= R_{22} - R_{11}\left[\frac{C_2}{3(b_1'-1)+2C_2}\right], \\ g &= \epsilon\rho^{-2C_{\epsilon 1}/3}. \end{aligned} \tag{30}$$

Here, the overbar on ρ is discarded to avoid potential conflict between Reynolds averaging and the sign of the exponent. Using mass conservation across the shock in the R_{11}, R_{22} and ϵ transport equations, we get the corresponding equations for f_1, f_2 and g that are devoid of non-conservative source terms, i.e., production and rapid pressure-strain. The transport equations given below, however represent identical physics as the original Equations (21), (7) and (28).

$$\begin{aligned} \frac{\partial}{\partial x}(\rho\widetilde{u}f_1) &= -\left(C_1 a_{11} + \frac{2}{3}\right)\rho g\rho^{2(b_1'-1)+2(C_{\epsilon 1}+2C_2)/3}, \\ \frac{\partial}{\partial x}(\rho\widetilde{u}f_2) &= -\widehat{C_1}\rho g\rho^{2C_{\epsilon 1}/3}, \\ \frac{\partial}{\partial x}(\rho\widetilde{u}g) &= -C_{\epsilon 2}\frac{\rho g^2}{k}\rho^{2C_{\epsilon 1}/3}, \end{aligned} \tag{31}$$

where the f_2 equation is written in compact form in terms of $\widehat{C_1} = [((3(1-b_1') - 2C_2)(3a_{22}C_1 - 2) + 3C_1C_2a_{11} + 2C_2)/(9(1-b_1') - 6C_2)]$. The model constants for the pressure-strain closure are given as $C_1 = 1$, and $C_2 = 0.55$, respectively. Here, a_{11} and a_{22} represents the anisotropy in Reynolds stresses, and b_1' is the shock-unsteadiness model coefficient given by Equation (20). The new transformed turbulent variables f_1, f_2 and g are conserved across the shock, if we neglect the dissipation effect on the RHS of Equation (31), as discussed above.

5. Simulation results

5.1. *Methodology*

The mean flow is solved by the one-dimensional Reynolds-averaged Navier–Stokes equations, and the f_1, f_2 and g equations (31) are solved for turbulence closure. All the equations are cast in non-dimensional form, where flow variables are normalized by the mean density and the mean speed of the sound, a_∞^*, taken at inlet station. The conservative form of the governing equations along with the turbulent transport equations are solved using a finite volume approach, where the conserved variables, U, inviscid fluxes, F, and source terms, S are written in vector form as,

$$\frac{\partial}{\partial t}\underbrace{\begin{bmatrix}\rho \\ \rho\widetilde{u} \\ \rho\widetilde{E} \\ \rho f_1 \\ \rho f_2 \\ \rho g\end{bmatrix}}_{U} + \frac{\partial}{\partial x}\underbrace{\begin{bmatrix}\rho\widetilde{u} \\ \rho\widetilde{u}^2 + \overline{p} + \rho R_{11} \\ \rho\widetilde{E} + \overline{p} \\ \rho\widetilde{u}f_1 \\ \rho\widetilde{u}f_2 \\ \rho\widetilde{u}g\end{bmatrix}}_{F} = \underbrace{\begin{bmatrix}0 \\ 0 \\ 0 \\ -\left(C_1a_{11} + \frac{2}{3}\right)\rho g\rho^{2(b_1'-1)+\frac{2}{3}(C_{\epsilon 1}+2C_2)} \\ -\widehat{C_1}\rho g\rho^{\frac{2C_{\epsilon 1}}{3}} \\ -C_{\epsilon 2}\frac{\rho g^2}{k}\rho^{\frac{2C_{\epsilon 1}}{3}}\end{bmatrix}}_{S}. \tag{32}$$

Here, $\widetilde{E}$ is the total mean energy and is given by $\frac{\overline{p}}{\gamma-1} + \frac{1}{2}\rho\widetilde{u}^2 + \rho k$ with $\gamma = 1.4$. The non-conservative form of the Reynolds stresses and the dissipation rate equations given by Equations (21), (7) and (28) are also written in a similar form for numerical implementation.

The equations consist of dimensionless and normalized quantities which are defined as, $x = x^*\kappa_0$, $t = t^*/(1/a^*_\infty\kappa_0)$, $\rho = \rho^*/\rho^*_\infty$, $u = u^*/a^*_\infty$, $T = T^*/T^*_\infty$, $R = R^*/(\gamma R^*)$, $p = p^*/(\rho^*_\infty a^{*2}_\infty)$, $R_{11} = R^*_{11}/a^{*2}_\infty$, $R_{22} = R^*_{22}/a^{*2}_\infty$, $R_{33} = R^*_{33}/a^{*2}_\infty$, $k = k^*/a^{*2}_\infty$, $\epsilon = \epsilon^*/a^{*3}_\infty\kappa_0$, where $(.)^*$ represents the dimensional values of flow variables and $(.)_\infty$ represents the shock upstream values. Here, t is time, T is temperature, and R^* is the specific gas constant and given as 287.1 J/Kg.K. The characteristic length scale is taken from the incoming turbulence field with peak wave number κ_0 of 4.

The inviscid fluxes are evaluated at the cell faces using the Lax-Friedrich (LF) scheme, and the turbulence source terms are evaluated at the cell centres. A fixed CFL value of 0.2 is maintained for all the numerical simulations. The LF scheme is first order accurate and more dissipative than the Steger-Warming (SW) scheme used in [15]. However, The SW results can be matched by using larger number of grid points in the LF simulations, as reported in [45, 46]. For the non-conservative formulation, the mean flow gradients in the production and the rapid pressure-strain terms are discretized using second order accurate central difference method.

The details of the domain, inlet, and boundary conditions are specified in Section 3.1. The initial conditions are given in table 1 for the non-conservative formulation. These are transformed to the new variables f_1, f_2 and g as per Equation (30). The same inlet values are specified at the upstream boundary and Rankine–Hugoniot jump relations of the mean flow quantities are used to set up the shock at $x = 0$. At the exit boundary, Neumann condition is used, i.e., the gradient of the conserved variables are maintained at zero. Explicit time integration is achieved using the forward Euler method with the given initial conditions.

5.2. *Turbulence Amplification across the shock*

Figure 6 shows the amplification of the Reynolds stresses, the turbulent dissipation rate and the Reynolds stress anisotropy across shock waves for varying upstream Mach number. Data for the baseline model are compared with the non-conservative and conservative forms of the present RSM based on shock-unsteadiness correction. The exact solution is obtained in the inviscid limit and the DNS data available are also presented for reference. The numerical solutions computed using the Lax–Friedrich scheme, where the mean flow variables across the shock are computed as part of the solution, are prone to numerical error at the shock wave. Similar results presented in figure 5, are obtained with hyperbolic tangent profiles prescribed for the mean flow variables across the shock. They do not have numerical errors typical of shock-capturing CFD simulations in figure 6, and isolate the physical modeling error in the models.

The numerical solution of the non-conservative formulation of the baseline as well as the present Reynolds stress model show a non-physical trend in the amplification of Reynolds stresses (see figures 6(a) and 6(b)). The post-shock Reynolds stresses for both cases are comparable to the DNS data and the exact integral solution for low Mach numbers up to about 1.5, indicating that the numerical errors are low for weak shock waves. In the range of Mach numbers from 1.5 to approximately 4.0, the models overpredict the Reynolds stresses, due to the large amplification of turbulence attributed to the non-conservative formulation of production and rapid pressure strain terms. There is a fall in R_{11} and R_{22} amplification beyond Mach

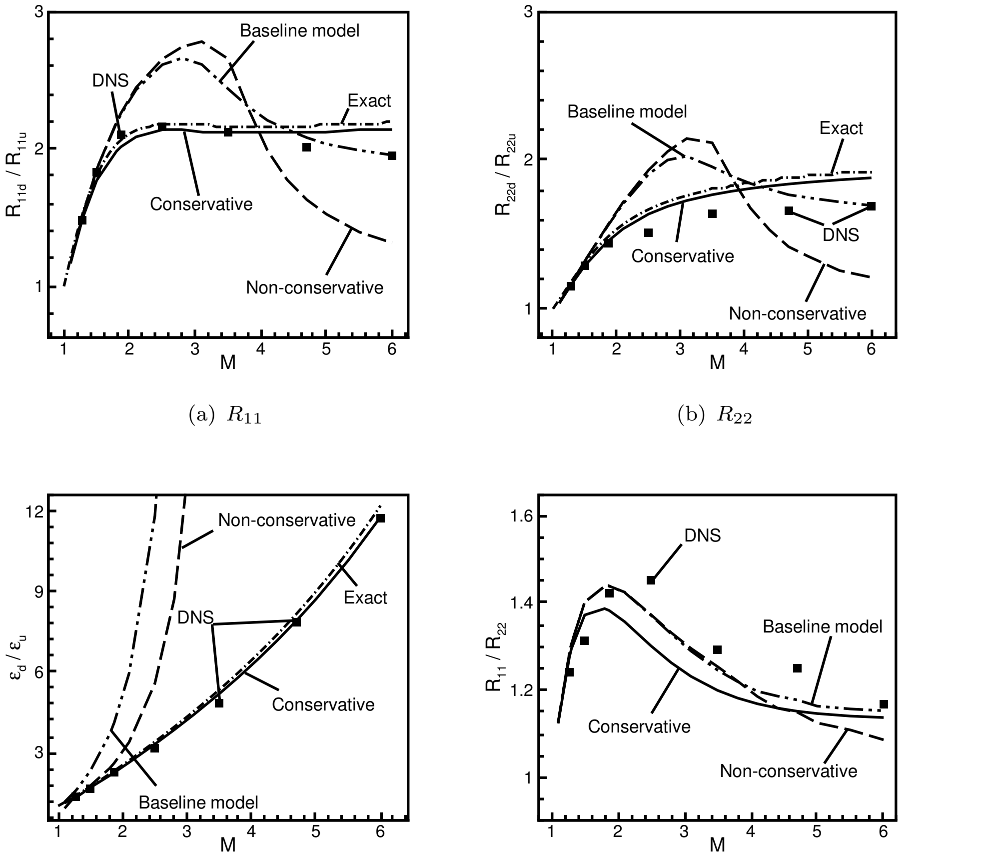

(a) R_{11}

(b) R_{22}

(c) ϵ

(d) R_{11}/R_{22}

Figure 6. The amplification in turbulent quantities across the shock obtained from the numerical simulation of the baseline model, the non-conservative and the conservative form of present model are compared with DNS data and the exact inviscid solution, for varying upstream Mach number. Solution computed on a 1000-point grid.

4, due to the excessively high turbulent dissipation rate predicted in the numerical simulation. For the strongest shock strengths (beyond Mach 4), the post-shock Reynolds stresses are underpredicted by the non-conservative model. With increasing Mach number, the non-monotonic trend of Reynolds stress amplifications is entirely due to the non-conservative numerical error at the numerically captured shock wave. The results obtained by numerically integrating the same model equations over pre-specified mean-flow shock profiles (see figure 5) are devoid of such numerical errors.

The post-shock dissipation rate of the baseline model and of the non-conservative form of the present RSM increases monotonically with increasing Mach numbers. They are much higher than the DNS data and the exact solution for all but the lowest Mach numbers. Similar results have been reported for the turbulent kinetic energy and its dissipation rate in Sinha and Balasridhar [15]. The amplification of the turbulent quantities computed using the conservative form of the present Reynolds stress model qualitatively follows the same trend as the exact inviscid solution. The results are also comparable to those presented in figure 5. R_{11} amplification (see figure 6(a)) shows a good match with DNS data except for a slight overprediction at high Mach numbers. The post-shock R_{22} of the conservative formulation also overpredicts the DNS data for Mach numbers beyond 2, but it is a significant improvement over the non-conservative results presented in figure 6(b).

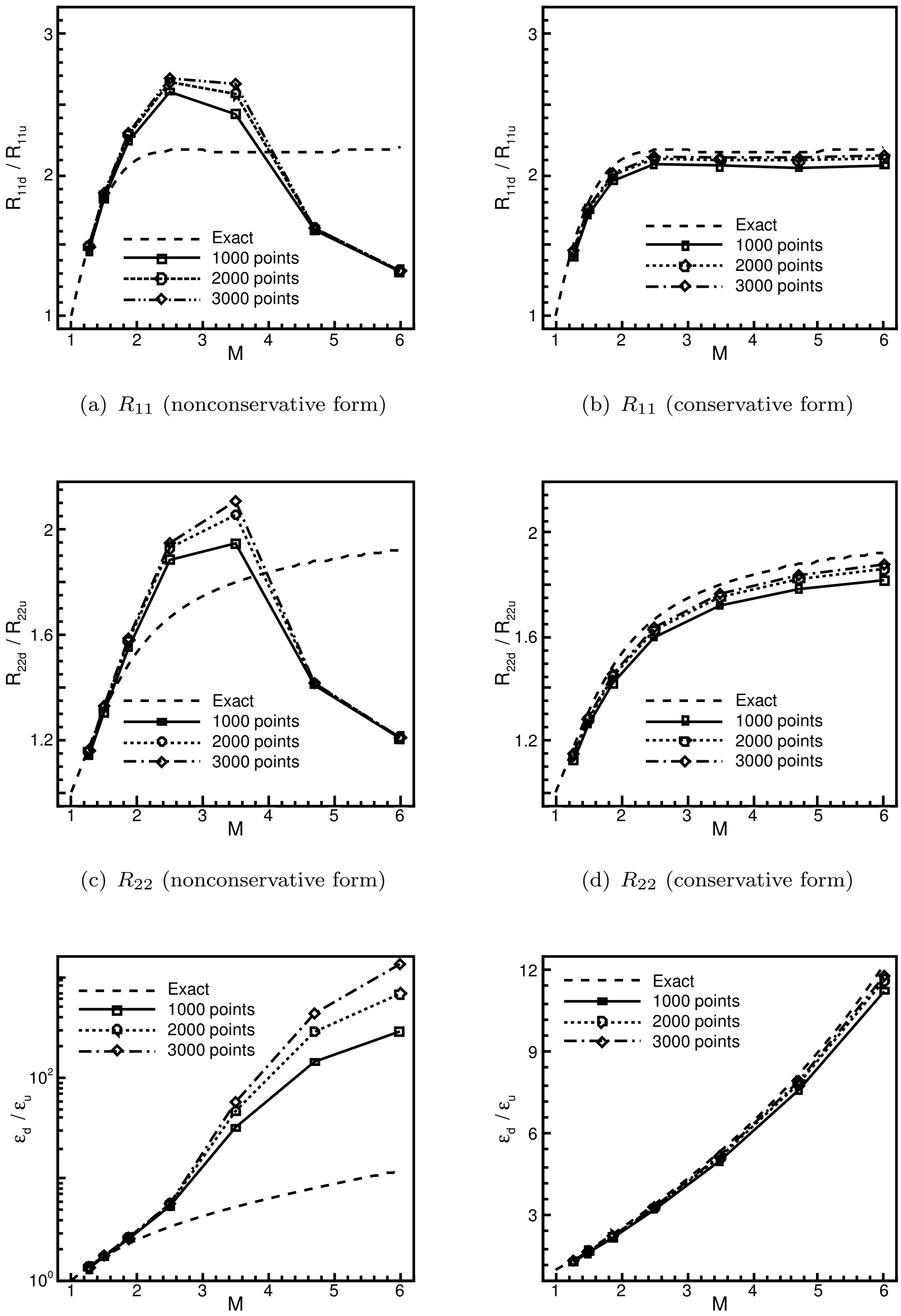

(a) R_{11} (nonconservative form)
(b) R_{11} (conservative form)
(c) R_{22} (nonconservative form)
(d) R_{22} (conservative form)
(e) ϵ (nonconservative form)
(f) ϵ (conservative form)

Figure 7. Effect of grid refinement on the amplification of the R_{11}, R_{22}, and ϵ with varying grid points for non-conservative and conservative form of the new RSM compared with exact integral solution.

The amplification of both the Reynolds stresses are marginally lower in magnitude than the exact inviscid solution, because of the dissipation effect in the shock region.

In figure 6(c), the post-shock dissipation rates of conservative formulation show a good match, both quantitatively and qualitatively, with the DNS data and the exact solution, for all Mach numbers. The anisotropy of the Reynolds stresses generated behind the shock shows the same qualitative behaviour for all the nu-

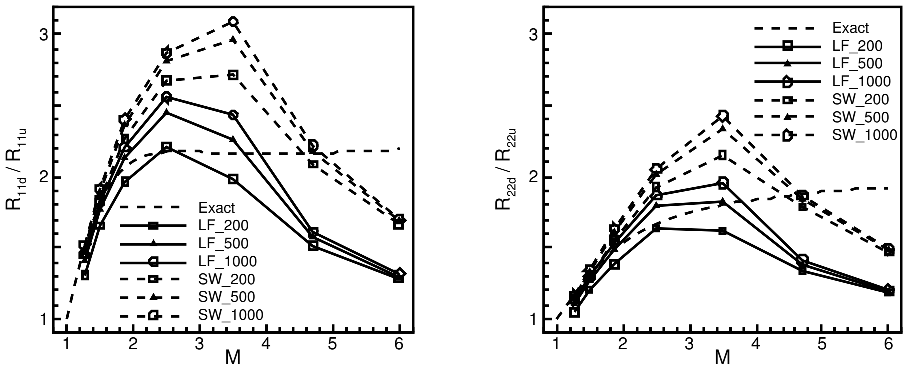

(a) R_{11} (b) R_{22}

Figure 8. Effect of numerical method on the amplification of the Reynolds stresses with grid refinement for non-conservative form of the new RSM.

merical solutions, and it matches the non-monotonic trend in the DNS data (see figure 6(d)). The conservative results underpredict R_{11}/R_{22} for much of the Mach number range, but is comparable to the DNS data for the strongest shock interaction. The non-conservative baseline and new model results appear to be closer to the DNS data, but they are more sensitive to the numerical grid, as will be discussed in the following text.

Figure 7 presents the numerical solutions computed using the non-conservative and conservative formulations of the new Reynolds stress model obtained using successively refined computational grids. Three grids with 1000, 2000, and 3000 points uniformly distributed over the computational domain have grid-cell sizes of 0.037, 0.018 and 0.012, respectively. The conservative results for R_{11}, R_{22}, and ϵ approach the exact inviscid solution as the shock gets thinner on finer grids and the effect of turbulent dissipation decreases with shock thickness. Note that molecular and turbulent diffusion terms are not included in the simulations, because their effect is found to be small in the region of the shock wave [45]. The conservative formulation also shows a converging trend towards a grid-independent solution. On the other hand, the non-conservative results (figures 7(a), 7(c) and 7(e)) retain the non-physical trends with successive grid refinement, and the numerical error is not found to decrease even on the finest grid. The turbulent dissipation rate results, plotted on a logarithmic scale, do not show a converging trend with successive grid refinement.

Figure 8 plots the amplification of Reynolds stresses obtained using different numerical schemes on much coarser meshes. The Lax-Friedrich method presented earlier is compared with Steger-Warming flux vector splitting approach, and the details of the method are presented in Sinha and Balasridhar [15]. Both the methods give qualitatively similar results, where the Reynolds stresses increase with Mach number, reach a maximum and then decrease for stronger shocks. The amplification factors obtained for the Steger Warming method are higher than the corresponding Lax-Friedrich results, and the increases further on grid-refinement. Application of different numerical schemes to the conservative formulation shows very little effect and is not presented here.

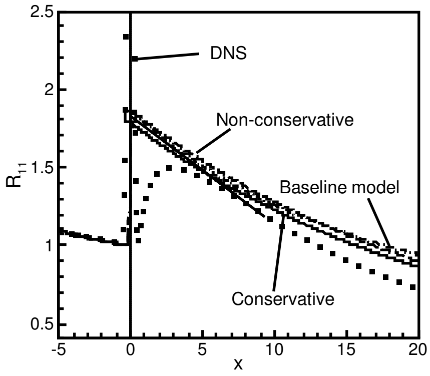

(a) R_{11}

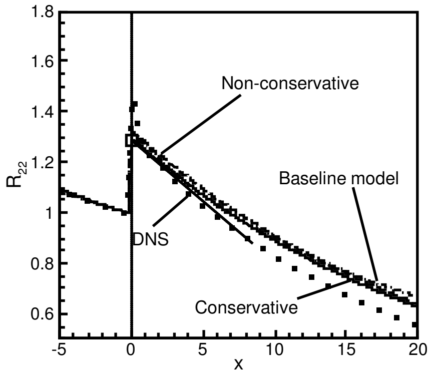

(b) R_{22}

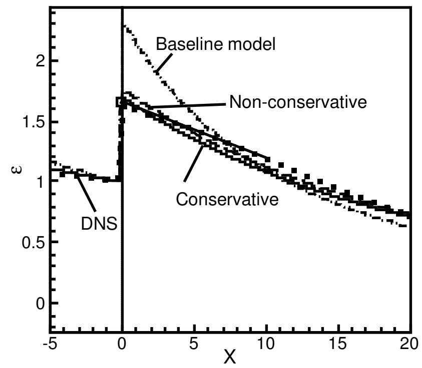

(c) ϵ

Figure 9. Streamwise evolution of the turbulence quantities in a Mach 1.5 canonical STI. Numerical solution computed using the Lax-Friedrich scheme for the baseline (dash-dot), the non-conservative form (long-dash) and the conservative form (solid-line) of the present RSM are compared with DNS data (symbol). The amplification in turbulent quantities obtained by extrapolation of the DNS data to mean shock location is shown by □.

5.3. *Streamwise evolution of Reynolds stressess*

Next, the streamwise evolution of turbulent quantities for the newly proposed Reynolds stress model and the baseline model are compared with the DNS data. Both non-conservative and conservative formulations are used in the simulations and the results are presented, along with DNS data, in figures 9–11. The turbulent quantities decay on either side of the shock and amplify across the shock wave due to a sudden change in mean velocity. The DNS data shows very large values of R_{11} in the region of the shock wave. This does not represent actual amplification of R_{11}, and is not captured by the turbulence models. There is a non-monotonic variation in the R_{11} immediately after the shock. This non-monotonic behaviour is due to the acoustic decay, as per by Mahesh *et al.* [11], and is not explicitly modeled in the present work. The post-shock DNS data is extrapolated back to the shock-center location ($x = 0$) to get an estimate of the effective jump (shown by an open square) in the turbulent quantities across the shock.

Figure 9 shows the streamwise evolution of the Reynolds stresses and the dissipation rate for Mach 1.5 shock-turbulence interaction. The amplification in R_{11} and R_{22} in all three solutions—baseline, non-conservative and conservative—are comparable to the DNS data extrapolated to the mean shock location of $x = 0$. The streamwise evolution of Reynolds stresses for non-conservative and conserva-

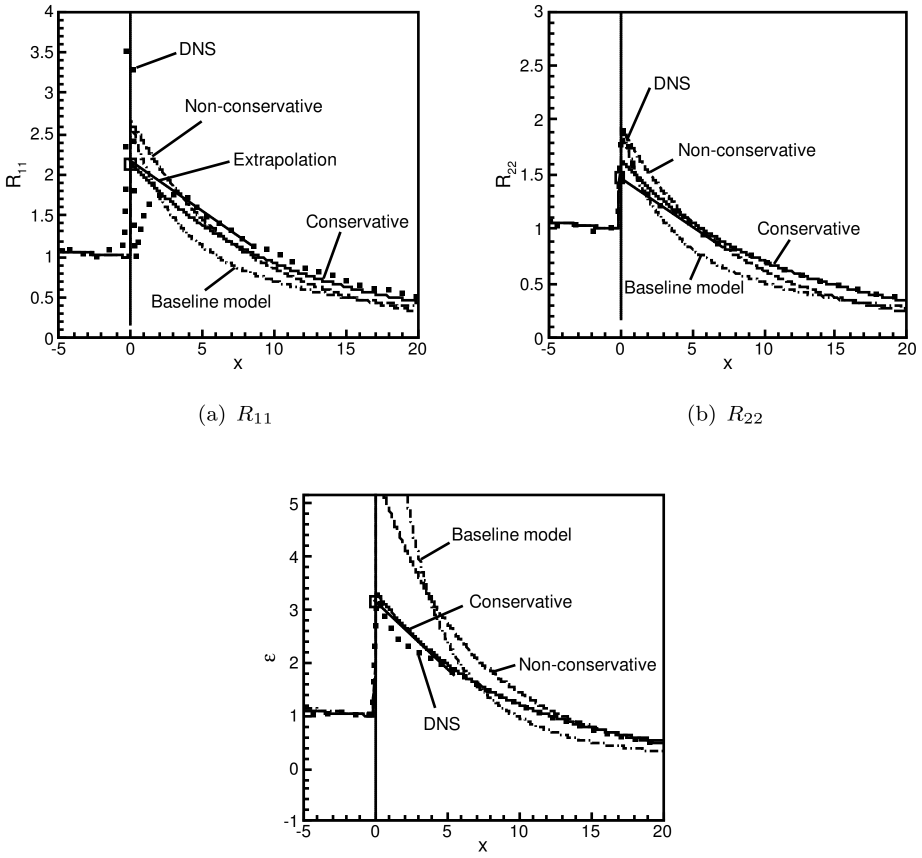

(a) R_{11} (b) R_{22}

(c) ϵ

Figure 10. Streamwise evolution of the turbulence quantities in a Mach 2.5 canonical STI. Numerical solution computed using the Lax-Friedrich scheme for the baseline (dash-dot), the non-conservative form (long-dash) and the conservative form (solid-line) of the present RSM are compared with DNS data (symbol). The amplification in turbulent quantities obtained by extrapolation of the DNS data to mean shock location is shown by □.

tive models decays monotonically and have an approximately same decay rate as that of baseline model both upstream and downstream of the shock wave. The models slightly underpredict the decay of the Reynolds stresses downstream of the shock in comparison with the DNS data. Here, the non-conservative and conservative RSMs show similar results indicating a small magnitude of numerical error for interaction with weak shock waves. The turbulent dissipation rate predictions show similar trends in figure 9(c), with the model results matching DNS data well. The only exception is the baseline model that gives too high an amplification in ϵ across the shock. For the Mach 2.5 case shown in figure 10, the best predictions are obtained using the conservative form of the new Reynolds stress model. The jump in R_{11} matches the extrapolated shock value in the DNS data. The R_{22} predictions match the DNS data over the entire domain, except for a small region immediately behind the shock. The turbulent dissipation rate matches the peak DNS value at the shock wave, overpredicts ϵ for $0 \leq x \leq 8$ and overlaps with DNS data further downstream. The trend is identical to that presented in Sinha [16], and this results in a slight underprediction of R_{11} in the downstream flow. The non-conservative simulation overpredicts R_{11}, R_{22}, and ϵ at the shock wave and exhibits a substantially higher post-shock decay rate than that in the DNS. The baseline model follows a similar trend, but the errors are higher than the non-conservative form

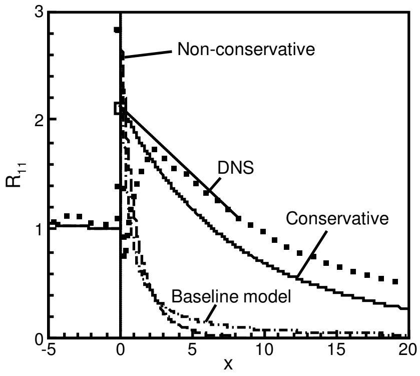

(a) R_{11}

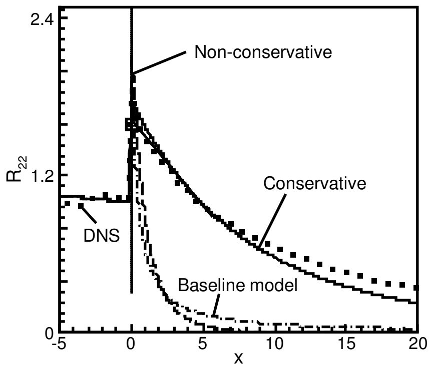

(b) R_{22}

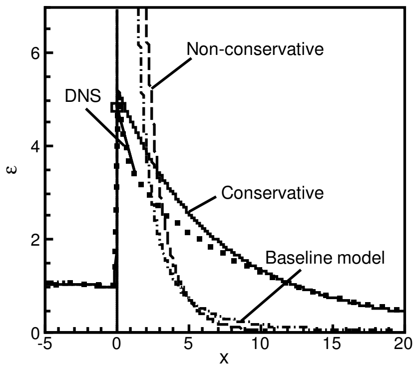

(c) ϵ

Figure 11. Streamwise evolution of the turbulence quantities in a Mach 3.5 canonical STI. Numerical solution computed using the Lax-Friedrich scheme for the baseline (dash-dot), the non-conservative form (long-dash) and the conservative form (solid-line) of the present RSM are compared with DNS data (symbol). The amplification in turbulent quantities obtained by extrapolation of the DNS data to mean shock location is shown by $\square$.

of the current RSM based on the shock-unsteadiness correction.

The non-conservative errors at the shock are even higher in the Mach 3.5 interaction presented in figure 11. In this case, the amplification of ϵ for the non-conservative and baseline models is higher than the DNS data by about an order of magnitude. It results in a rapid decay of the post-shock turbulence, which is very different from the trend observed in the DNS. The conservative model (with minimal numerical and physical modeling error), once again, is the closest to the DNS data. The shock-jumps in R_{11}, R_{22}, and ϵ are reproduced well by the new model, but the decay rate of the Reynolds stresses is overpredicted, due to the turbulent dissipation rate being higher than DNS data in the range $0 < x < 8$.

6. Generalization to multi-dimensional problems

The results presented above show that a physically consistent and numerically robust Reynolds stress model is able to predict the changes across a normal shock. For an oblique shock oriented at a angle θ in the $x - y$ plane (shown in figure 12), the proposed model equations for R_{11}, R_{22} can be interpreted in terms of the shock-normal $R_{\eta\eta}$ and transverse $R_{\xi\xi}$ components. Equation (21) can thus be

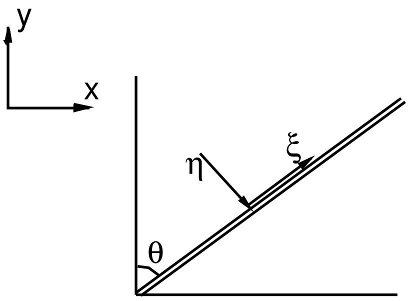

Figure 12. Schematic of an oblique shock at an angle θ to the y-coordinate in the lab frame of reference.

written in a general tensor form as

$$\frac{D\overline{\rho}R_{\eta\eta}}{Dt} = (2(b_1' - 1) + \frac{4}{3}C_2)\overline{\rho}R_{\eta\eta}\frac{\partial \widetilde{u}_k}{\partial x_k} - C_1\overline{\rho}\epsilon a_{\eta\eta} - \frac{2}{3}\overline{\rho}\epsilon, \tag{33}$$

where $a_{\eta\eta}$ is the anisotropy in the shock-normal Reynolds stress. Note that the mean derivatives in the shock-transverse directions are assumed to be small such that the shock-normal velocity gradient on the right-hand side is replaced by the mean dilatation. Similarly, the shock-normal convection term on the left-hand side is generalized to the material derivative.

Following identical procedure for the shock-transverse Reynolds stress $R_{\xi\xi}$, we generalize Equation (7) to

$$\frac{D\overline{\rho}R_{\xi\xi}}{Dt} = -\frac{2}{3}C_2\overline{\rho}R_{\eta\eta}\frac{\partial \widetilde{u}_k}{\partial x_k} - C_1\overline{\rho}\epsilon a_{\xi\xi} - \frac{2}{3}\overline{\rho}\epsilon. \tag{34}$$

where $a_{\xi\xi}$ is the anisotropy in the transverse Reynolds stress. For the Reynolds stress component R_{12}, we start with Equation (1) written for a shock wave normal to the x-direction,

$$\frac{\partial \overline{\rho}\widetilde{u}R_{12}}{\partial x} = (C_2 - 1)\overline{\rho}R_{12}\frac{\partial \widetilde{u}}{\partial x} - C_1\overline{\rho}\epsilon a_{12}, \tag{35}$$

and generalize it to an oblique shock to get the model transport equation for the Reynolds stress component $R_{\eta\xi}$

$$\frac{D\overline{\rho}R_{\eta\xi}}{Dt} = (C_2 - 1)\overline{\rho}R_{\eta\xi}\frac{\partial \widetilde{u}_k}{\partial x_k} - C_1\overline{\rho}\epsilon a_{\eta\xi}. \tag{36}$$

where $a_{\eta\xi}$ is the anisotropy in the Reynolds stress component $R_{\eta\xi}$.

The Reynolds stresses in the lab frame of reference (x, y) can be related to those in the shock frame by the coordinate transformation

$$\begin{aligned}
R_{11} &= cos^2\theta R_{\eta\eta} + sin2\theta R_{\eta\xi} + sin^2\theta R_{\xi\xi}, \\
R_{22} &= sin^2\theta R_{\eta\eta} - sin2\theta R_{\eta\xi} + cos^2\theta R_{\xi\xi}, \\
R_{12} &= (R_{\xi\xi} - R_{\eta\eta})cos\theta sin\theta + (cos^2\theta - sin^2\theta)R_{\eta\xi}.
\end{aligned} \tag{37}$$

The transport equations for R_{11}, R_{22} and R_{12} can now be derived in terms of the model equations for $R_{\eta\eta}$, $R_{\xi\xi}$ and $R_{\eta\xi}$ given above. On simplification, we get

$$\frac{D\overline{\rho}R_{11}}{Dt} = (A_{11}\overline{\rho}R_{11} + A_{12}\overline{\rho}R_{22} + A_{13}\overline{\rho}R_{12})\frac{\partial\widetilde{u_k}}{\partial x_k} - C_1\overline{\rho}\epsilon a_{11} - \frac{2}{3}\overline{\rho}\epsilon, \quad (38)$$

$$\frac{D\overline{\rho}R_{22}}{Dt} = (A_{21}\overline{\rho}R_{11} + A_{22}\overline{\rho}R_{22} + A_{23}\overline{\rho}R_{12})\frac{\partial\widetilde{u_k}}{\partial x_k} - C_1\overline{\rho}\epsilon a_{22} - \frac{2}{3}\overline{\rho}\epsilon, \quad (39)$$

$$\frac{D\overline{\rho}R_{12}}{Dt} = (A_{31}\overline{\rho}R_{11} + A_{32}\overline{\rho}R_{22} + A_{33}\overline{\rho}R_{12})\frac{\partial\widetilde{u_k}}{\partial x_k} - C_1\overline{\rho}\epsilon a_{12}, \quad (40)$$

where the reverse transformation is used to express $R_{\eta\eta}$, $R_{\xi\xi}$ and $R_{\eta\xi}$ on the right-hand side in terms of R_{11}, R_{22} and R_{12}. The model coefficients in the above equations are as follows,

$$A_{11} = (-2 + 2b_1' + \frac{4}{3}C_2)cos^4\theta - \frac{2}{6}C_2 sin^2 2\theta + \frac{(C_2-1)}{2}sin^2 2\theta,$$

$$A_{12} = (-1 + b_1' + \frac{4}{6}C_2)sin^2 2\theta - \frac{2}{3}C_2 sin^4\theta - \frac{(C_2-1)}{2}sin^2 2\theta,$$

$$A_{13} = \left((2 - 2b_1' + \frac{4}{3}C_2)cos^2\theta + \frac{2}{3}C_2 sin^2\theta\right) sin2\theta + \frac{(C_2-1)}{2}sin4\theta,$$

$$A_{21} = (-1 + b_1' + \frac{4}{6}C_2)sin^2 2\theta - \frac{2}{3}C_2 cos^4\theta - \frac{(C_2-1)}{2}sin^2 2\theta,$$

$$A_{22} = (-2 + 2b_1' + \frac{4}{3}C_2)sin^4\theta - \frac{2}{6}C_2 sin^2 2\theta + \frac{(C_2-1)}{2}sin^2 2\theta,$$

$$A_{23} = \left((2 - 2b_1' - \frac{4}{3}C_2)sin^2\theta + \frac{2}{3}C_2 cos^2\theta\right) sin2\theta - \frac{(C_2-1)}{2}sin4\theta,$$

$$A_{31} = (1 - b_1' - C_2)sin2\theta cos^2\theta + \frac{(C_2-1)}{4}sin4\theta,$$

$$A_{32} = (1 - b_1' - C_2)sin2\theta sin^2\theta + \frac{(C_2-1)}{4}sin4\theta,$$

$$A_{33} = (1 - b_1' - C_2)sin^2 2\theta + (C_2-1)cos^2 2\theta$$

The Reynolds stress R_{33} is transverse to the oblique shock defined in figure 12. It behaves akin to $R_{\xi\xi}$ across the shock wave and the model transport equation takes the form

$$\frac{D\overline{\rho}R_{33}}{Dt} = -\frac{2}{3}C_2\overline{\rho}R_{\eta\eta}\frac{\partial\widetilde{u}_k}{\partial x_k} - C_1\overline{\rho}\epsilon a_{33} - \frac{2}{3}\overline{\rho}\epsilon,$$

which is derived from Equation (34), and can be written as,

$$\frac{D\overline{\rho}R_{33}}{Dt} = -\frac{2}{3}C_2\overline{\rho}\left(cos^2\theta R_{11} - sin2\theta R_{12} + sin^2\theta R_{22}\right)\frac{\partial\widetilde{u}_k}{\partial x_k} - C_1\overline{\rho}\epsilon a_{33} - \frac{2}{3}\overline{\rho}\epsilon, \quad (41)$$

Finally, the dissipation rate Equation (28) is cast in general tensor form as,

$$\frac{D\overline{\rho}\epsilon}{Dt} = -\frac{2}{3}C_{\epsilon 1}\overline{\rho}\epsilon\frac{\partial\widetilde{u}_k}{\partial x_k} - C_{\epsilon 2}\overline{\rho}\frac{\epsilon^2}{k}. \quad (42)$$

The above five Equations (38-42) represent a physically consistent Reynolds stress model for flows with shock waves oriented at an angle θ in the $x-y$ plane. The equations can be further generalized for shock waves with any arbitrary orientation in a three-dimensional flow.

An existing CFD code can be modified to implement these equations in regions of shock wave, identified in terms of large negative values of mean dilatation. A shock detector function can be used [8, 18] such that the modifications are restricted to high-compression regions, without altering the base model in the flow outside of shock waves. The shock angle θ can be calculated using the local mean pressure gradient vector. The model coefficients depend on θ, which is physically consistent with the directional nature of a shock wave. A shock alters the normal and transverse Reynolds stresses differently and this information is retained in the new physics-based RSM. The local pressure gradient can also be used to obtain the shock-normal component of the Mach number. This has been successfully implemented in SBLI flows with a single oblique shock [8] and with multiple shock waves [18]. Newer approaches which eliminate the dependence of the model coefficient b_1' on M_{1n} are also being explored [46].

We note that the above RSM equations (38-42) for a shock wave are in non-conservative form. They are expected to give accurate prediction for shock with M_{1n} upto 1.5 (see figure 9) and possibly as high as $M_{1n} = 2$. The corresponding upstream flow Mach number can be much higher (up to $M = 5$) for weak oblique shocks. For stronger shock waves, we need to employ a conservative formulation to eliminate large numerical error at the shock discontinuity. This is achieved by writing the conserved variables f_1, f_2 and g, in Equation (31), in terms of the shock-normal and transverse Reynolds stresses.

$$\begin{aligned} f_1 &= R_{\eta\eta}\rho^{\alpha_1}, \\ f_2 &= R_{\xi\xi} - \beta R_{\eta\eta}, \\ f_3 &= R_{\eta\xi}\rho^{(1-C_2)}, \\ g &= \epsilon\rho^{-2C_{\epsilon 1}/3}, \end{aligned} \tag{43}$$

where $\alpha_1 = 2(b_1' - 1) + 4C_2/3$ and $\beta = 2C_2/3\alpha_1$, and a new conserved variable f_3 is defined for the Reynolds stress component $R_{\eta\xi}$. Here, the overbar on ρ is discarded to avoid potential conflict between Reynolds averaging and the sign of the exponent. The model transport equations for the conserved variables, Equation (31) can be generalized to

$$\frac{D(\rho f_1)}{Dt} = -(C_1 a_{\eta\eta} + \frac{2}{3})\rho g \rho^{\alpha_1 + 2C_{\epsilon 1}/3}, \tag{44}$$

$$\frac{D(\rho f_2)}{Dt} = -\widehat{C_1}\rho g \rho^{2C_{\epsilon 1}/3}, \tag{45}$$

$$\frac{D(\rho f_3)}{Dt} = -C_1 a_{\eta\xi}\rho g \rho^{1-C_2+2C_{\epsilon 1}/3}, \tag{46}$$

$$\frac{D(\rho g)}{Dt} = -C_{\epsilon 2}\frac{\rho g^2}{k}\rho^{2C_{\epsilon 1}/3}, \tag{47}$$

where $\widehat{C_1}$ is in terms of $a_{\eta\eta}$ and $a_{\xi\xi}$, and the diffusion terms are neglected at the shock wave.

The Reynolds stresses R_{11}, R_{22}, and R_{12} available upstream of a shock wave can be rotated to the shock coordinate system (shown in figure 12).

$$\begin{aligned} R_{\eta\eta} &= cos^2\theta R_{11} - sin2\theta R_{12} + sin^2\theta R_{22}, \\ R_{\xi\xi} &= sin^2\theta R_{11} + sin2\theta R_{12} + cos^2\theta R_{22}, \\ R_{\eta\xi} &= (R_{11} - R_{22})cos\theta sin\theta + (cos^2\theta - sin^2\theta)R_{12}, \end{aligned} \tag{48}$$

which can then be used to arrive at the upstream values of the conserved variables, as per Equation (43). The post-shock values obtained by solving Equations (44)-(47) across the shock can then be converted back to R_{11}, R_{22}, and R_{12} by invoking the reverse transformation.

The R_{33} equation not included in the above discussion can be transformed to a conservative form by following a similar approach. The resulting RSM equations can be used effectively for the entire range of Mach numbers. Application of the generalized model to realistic flows like shock-boundary layer interaction is beyond the scope of the current work.

7. Conclusion

In this work, we study the variation of Reynolds stresses when homogeneous isotropic turbulence interacts with a nominally normal shock wave. The transport equations of the existing Reynolds stress models are simplified for a steady one-dimensional mean flow, and integrated to yield the jump in the normal Reynolds stresses across the shock. Comparison with available DNS data shows significant over prediction in the amplification of the streamwise and transverse Reynolds stresses. This could possibly be because of the fact that the existing models do not account for the damping effect of unsteady shock oscillations. Sinha *et al.* [14] developed a model for the shock-unsteadiness effect based on theoretical analysis of canonical shock-turbulence interaction. The model was found to predict the amplification of turbulence kinetic energy across the shock accurately, and has shown good potential in shock-boundary layer interaction flows. We incorporate the shock-unsteadiness model in the Reynolds stress transport equation, and it is found to significantly improve the post-shock Reynolds stress predictions. The dissipation rate equation is also modified based on the variation of enstrophy and mean kinematic viscosity across a shock wave, as per Sinha [16].

The new physics-based Reynolds stress model thus obtained is used to predict canonical shock-turbulence interaction, for which DNS data is available in literature. The current predictions show significant improvement over existing models, for both streamwise and transverse Reynolds stresses. The jump in the turbulence quantities and their downstream evolution matches DNS data well for Mach numbers ranging from low supersonic to the hypersonic regime. Further, the model is able to reproduce the non-monotonic variation of Reynolds stress anisotropy behind the shock with increasing shock strength. The new model equations for the normal Reynolds stresses, along with the transport equations for the Reynolds shear stress, are generalized to a tensor form that can be applied to multi-dimensional flows with shock waves of arbitrary orientation.

The model equations, when implemented in a CFD code, exhibit large numerical error at flow discontinuities like shock waves. This is due to the non-conservative source terms in the transport equations, which take un-physical values in a shock. We propose a novel transformation of the Reynolds stresses and the turbulent dissipation rate into new turbulence variables that are conserved across a shock.

This minimizes numerical error and gives well-behaved results, which converge to closed-form analytical solution on successive grid refinement. The new Reynolds stress model equations are thus physically consistent and numerically robust for modeling high-speed turbulent flows with shock waves.

References

[1] A. A. Zheltovodov, *Some advances in research of shock wave turbulent boundary layer interactions*, AIAA Paper. 496 (2006), pp. 1–25.

[2] C. J. Roy, and F. G. Blottner, *Review and assessment of turbulence models for hypersonic flows*, Progress in Aeropsace Sciences. 42 (2006), pp. 469-530.

[3] D. Gaitonde, *Progress in shock wave/boundary layer interactions*, Prog Aerosp Sci. 72 (2015), pp. 80–99.

[4] B. Morgan, K. Duraisamy, N. Nguyen, S. Kawai, and S. K. Lele, *Flow physics and RANS modelling of oblique shock/turbulent boundary layer interaction*, Journal of Fluid Mechanics. 79 (2013), pp. 231–284.

[5] P. E. Hamlington, and W. J. A. Dahm, *Reynolds Stress Closure for Nonequilibrium Eects in Turbulent Flows*, Physics of Fluids. 20 (2008), 1151101.

[6] R. F. Vieira, and J. L. F. Azevedo, *Turbulence Model Assessment for Simulation of Shock Wave-Boundary Layer Interaction Flows*, 31st AIAA Applied Aerodynamics Conference, 2013, 3024.

[7] J. Liu, and Z. Zhao, *Reynolds-Stress Turbulence Models for Hypersonic ShockWave/Turbulent-Boundary-Layer Interactions* , AIAA SPACE Conference and Exposition, 2014, 4413.

[8] K. Sinha, K. Mahesh, and G. V. Candler, *Modeling the effect of shock unsteadiness in shock/turbulent boundary layer interactions*, AIAA Journal. 43 (2005), 586594.

[9] J. Larsson, and S. K. Lele, *Direct numerical simulation of canonical shock / turbulence interaction*, Physics of Fluids. 21 (2009), 126101.

[10] J. Larsson, I. Bermejo-Moreno, and S. K. Lele, *Reynolds- and Mach-number effects in canonical shock-turbulence interaction*, Journal of Fluid Mechanics. 717 (2013), pp. 293–321.

[11] K. Mahesh, S. K. Lele, and P. Moin, *The influence of entropy fluctuations on the interaction of turbulence with a shock wave*, Journal of Fluid Mechanics. 334 (1997), pp. 353–379.

[12] P. A. Durbin, and O. Zemen, *Rapid distortion theory for homogeneous compressed turbulence with application to modelling*, Journal of Fluid Mechanics. 242 (1992), pp. 349–370.

[13] J. Wouchuk, C. Huete Ruiz de Lira, and A. Velikovich, *Analytical linear theory for the interaction of a planar shock wave with an isotropic turbulent vorticity field*, Physics Review E. 79 (2009), 066315.

[14] K. Sinha, K. Mahesh, and G. V. Candler, *Modeling shock unsteadiness in shock/turbulence interaction*, Physics of Fluids. 15 (2003), 2290.

[15] K. Sinha, and S. J. Balasridhar, *Conservative formulation of the $k-\epsilon$ turbulence model for shock-turbulence interaction*, AIAA Journal. 51 (2013), pp. 1872–1882.

[16] K. Sinha, *Evolution of enstrophy in shock/homogeneous turbulence interaction*, Journal of Fluid Mechanics. 707 (2012), pp. 74–110.

[17] V. K. Veera, and K. Sinha, *Modeling the effect of upstream temperature fluctuations on shock/homogeneous turbulence interaction*, Physics of Fluids. 2 (2009), pp. 025101.

[18] A. A. Pasha, and K. Sinha, *Shock-unsteadiness model applied to oblique shock wave/turbulent boundary layer interaction*, International Journal of Computational Fluid Dynamics. 22 (2008), 569–582.

[19] A. A. Pasha, and K. Sinha, *Simulation of hypersonic shock/turbulent boundary-layer interactions using shock-unsteadiness model*, Journal of Propulsion and Power. 28 (2012), 4660.

[20] J. C. Rotta, *Statistich theorie nichthomogener turbulenz I*, Zeitschrift fur physik. 129 (1951), pp. 547–573.

[21] B. E. Launder, G. J. Reece, and W. Rodi, *Progress in the development of a Reynolds-stress turbulence closure*, Journal of Fluid Mechanics. 68 (1975), pp. 537–566.

[22] J. L. Lumley, *Turbulence modeling* , Advance of Applied mechanics. 18 (1978).

[23] C. G. Speziale, S. Sarkar, and T. B. Gatski, *Modelling the pressure-strain correlation of turbulence: an invariant dynamical systems approach* , Journal of Fluid Mechanics. 227 (1991), pp. 245–272.

[24] M. M. Gibson, and B. E. Launder, *Ground effects on pressure fluctuations in the atmospheric boundary layer* , Journal of Fluid Mechanics. 86 (1978), pp. 491–511.

[25] B. E. Launder, and N. Shima, *Second-Moment Closure for the Near-Wall Sublayer : Development and Application*, AIAA Journal. 27 (1989), pp. 1319–1325.

[26] G. A. Gerolymos, E. Sauret, and I. Vallet, *Contribution to the single-point-closure Reynolds-stress modelling of inhomogeneous flow*, Theor. Comput. Fluid Dyn. 17 (2004), pp. 407–431.

[27] G. A. Gerolymos, and I. Vallet, *Wall-normal-free near-wall Reynolds-stress closure for 3-D compressible separated flows*, AIAA Journal. 39 (2001), pp. 1833–1842

[28] G. A. Gerolymos, C. Lo, I. Vallet, and B. A. Younis, *Term-by-term analysis of near-wall second moment closures*, AIAA Journal. 50 (2012), pp. 2848–2864.

[29] G. A. Gerolymos, E. Sauret, and I. Vallet, *Oblique-Shock-Wave/Boundary-Layer Interaction Using Near-Wall Reynolds Stress Models*, AIAA Journal. 42 (2004), pp. 1089–1100.

[30] B. E. Launder, and B. I. Sharma, *Application of the energy-dissipation model of turbulence to the calculation of flow near a spinning disc*, Letters in Heat and Mass Transfer. 1(1974), pp. 131–137.

[31] G. A. Gerolymos, and I. Vallet, *Near-wall Reynolds stress three dimensional transonic flow computation*, AIAA Journal. 35 (1997), pp. 228–236.

[32] E. Sauret, and I. Vallet, *Near-wall turbulent pressure diffusion modelling and influence in 3-D secondary flows*, ASME J. Fluids Eng. 129 (2007), pp. 634–642.

[33] I. Vallet, *Reynolds-stress modelling of M= 2.25 shock-wave/turbulent-boundary-layer interaction*, Int J. Numer. Methods Fluids. 56 (2008), pp. 525–555.

[34] J. Lee, D. B. Taulbee, and M.S. Holden, *Study of Turbulence on Supersonic Compression Surfaces Using Reynolds Stress Model*, AIAA Journal 30. (1992), pp. 1738–1746.

[35] F. Ladiende, *Supersonic flux-split procedure for second moments of turbulence*, AIAA Journal. 33 (1995), pp. 1185–1195.

[36] M. Gnedin, and Doyle Knight, *A Reynolds stress equation turbulence model for compressible flows, Part-I: Flat plate boundary layers*, AIAA Journal. (1995).

[37] C. Pantano, and S. Sarkar, *A study of compressibility effects in the high-speed turbulent shear layer using direct simulation*, Journal of Fluid Engineering. 451 (2002), pp. 329–371.

[38] O. Zeman, *Dilatational dissipation: The concept and application in modeling compressible mixing layers*, Phys. Fluids A. 2(1992), pp. 178–188.

[39] G. C. Zha, and D. Knight, *Three-Dimensional Shock / Boundary-Layer Interaction Using Reynolds Stress Equation Turbulence Model*, AIAA Journal. 34 (1996), pp. 1313–1320.

[40] D. C. Wilcox, *Turbulence Modelling for CFD*, DCW industries, Inc. (2000).

[41] B. J. Daly, and F. H. Harlow, *Transport Equations in Turbulence*, Phys. Fluids. 13 (1970), pp. 2635–2649.

[42] D. Souffland, O. Soulard, and J. Griffond, *Modeling of Reynolds stress models for diffusion fluxes inside shock waves*, Journal of Fluid Engineering. 136 (2014), 091102-1–091102-4.

[43] B. M. Johnson, and O. Schilling, *Reynolds-averaged Navier-Stokes model predictions of linear instability.II.Shock-driven* , Journal of Turbulence. 12 (2011), pp. 1–31.

[44] J. Griffond, and S. Olivier, *Evaluation of augmented RSM for interaction of homogeneous turbulent mixtur with shock and rarefraction waves*, Journal of Turbulence. 15 (2014), pp. 569–595.

[45] K. Sinha, and R. Singh, *Numerical Error in the $k-\epsilon$ Turbulence Model applied to Eddy-viscous Shock Waves*, AIAA Journal. (2016).

[46] P. Raje, and K. Sinha, *A physically consistent and numerically robust $k-\epsilon$ model for computing turbulent flows with shock waves*, Computers & Fluids. 136 (2016), pp. 35–47.

[47] R. Quadros, K. Sinha, and J. Larsson, *Turbulent energy flux generated by shock/homogeneous-turbulence interaction*, Journal of Fluid Mechanics. 796 (2016), pp. 113–57.